Preemptive glycogen storage in granulosa cells powers avascular corpus luteum via glycogenolytic energy provision

Jianning Liao[1†], Qinghua Liu[1,7†], Cong Liu[2†], Guiqiong Liu[1†], Xiang Li[1†], Xiaodong Wang[1], Yaqin Wang[2], Ruiyan Liu[1], Hao Wu[3], Chaoli Wang[5], Hongru Shi[1], Yongheng Zhao[1], Wenkai Ke[1], Zaohong Ran[1], Zian Wu[1], Bowen Tan[1], Quanfeng Wang[6], Guohua Hua[1], Shujun Zhang[1], Qingzhen Xie[2*], Guoshi Liu[3*], Changjiu He[1,4*]

[1] Key Laboratory of Agricultural Animal Genetics, Breeding and Reproduction of Ministry of Education, College of Animal Sciences and Technology, Huazhong Agricultural University, Wuhan 430070, PR China;

[2] Centre for Reproductive Medicine, Renmin Hospital of Wuhan University, Wuhan 430000, China;

[3] Key Laboratory of Animal Genetics and Breeding of the Ministry of Agriculture, College of Animal Science and Technology, China Agricultural University, Beijing, China;

[4] College of Animal Science and Technology, Shihezi University, Shihezi, China;

[5] Xinjiang Western Animal Husbandry Co., Ltd, Shihezi, China;

[6] Xinjiang Jinken aoqun agriculture and animal husbandry technology Co., Ltd, Hetian, China;

[7] Binzhou Bincheng District Animal Husbandry and Veterinary Service Center, Binzhou, China.

[†] These authors contributed equally to this work.

***Corresponding Author**:

Changjiu He,

Orcid ID: 0000-0002-0350-9799;

Email: chungjoe@mail.hzau.edu.cn; Huazhong Agricultural University, Wuhan 430070, China.

Guoshi Liu,

Orcid ID: 0000-0002-5688-3645;

Email: gshliu@cau.edu.cn; China Agricultural University, Beijing 100193, China

Qingzhen Xie,

Orcid ID: 0000-0002-4628-4278;

Email: rm001138@whu.edu.cn; Renmin Hospital of Wuhan University, Wuhan 430000, China.

Short title: GCs store glycogen for corpus luteum

ABSTRACT

The corpus luteum (CL) arises from the luteinization of follicular granulosa cells (GCs) and theca cells, marked by rapid progesterone elevation and angiogenesis. Intriguingly, angiogenesis lags behind progesterone elevation, creating an avascular phase during which luteal cells must fuel intensive steroidogenesis without perfusion. How the avascular CL meets this energetic demand remains a mystery. Here, we reveal a novel cellular adaptive mechanism–GC energy storage (GCES)–that resolves this enigma. We demonstrate that upon luteinization initiation, GCs enter a metabolically quiescent state yet enhance glucose uptake via SLC2A1, converting the glucose into glycogen through the hCG (LH)-MAPK-RUNX1-Insulin signaling axis. Catabolism of this glycogen reserve supplies the energy required for the avascular CL, ensuring normal luteogenesis. GCES is evolutionarily conserved across species. Genetic or pharmacological disruption of GCES or glycogenolysis induces luteal insufficiency, whereas timely glucose administration enhances GCES, improving luteal function and optimize reproductive outcome in both mouse and ovine models. In human study, orally intake of glucose post-hCG significantly augments GCES and enhances progesterone production in women. These results advance luteal physiology by uncovering a universal reproductive principle with direct clinical implications.

Keywords: ovulation, glycogen, granulosa cell, corpus luteum, follicle, luteinization.

54 **INTRODUCTION**

55 The corpus luteum (CL) is a temporary ovarian endocrine structure critical for
56 reproduction. It sustains pregnancy by secreting progesterone and orchestrates the
57 reproductive cycle via its cyclic formation and regression [1, 2]. Luteal insufficiency,
58 defined by the suboptimal progesterone production and shortened luteal phase,
59 represents a common etiology of female subfertility and is closely linked to
60 reproductive disorders, including menstrual disorders, premenstrual spotting and
61 recurrent pregnancy loss [3, 4]. It is estimated that ~8% of reproductive-age women
62 experience luteal insufficiency, with the incidences escalating in parallel to maternal
63 age [3, 5-8]. Notably, luteal insufficiency is prevalent in recurrent miscarriage cases [9,
64 10], underscoring its profound impact on reproductive health.

65 CL arises from the luteinization of granulosa cells (GCs) and theca cells, a process
66 triggered by the pre-ovulatory surge of luteinizing hormone (LH) or human chorionic
67 gonadotropin (hCG, an LH-equivalent hormone) [11]. Luteinization encompasses
68 multiple coordinated cellular mechanisms, such as proliferation cessation,
69 steroidogenesis reprogramming, GC-layer stiffening, cell migration and
70 neovascularization [2, 12-15]. LH (hCG)-activated downstream regulators, including
71 P21CIP1, P27KIP1, ERK1/2, PI3K/AKT, CEBPα/β, RUNX1/2, NR4A2/NURR1,
72 CREB, cortisol/glucocorticoid receptors and H3K27me3/H3K9me3 [16-25],
73 collectively regulate luteinization.

74 Although derived from GCs, luteal cells exhibit a markedly elevated progesterone
75 synthesis capacity, exceeding that of their GC precursors by several orders of
76 magnitude [26]. This metabolic upscaling renders the CL one of the most highly
77 vascularized and energetically demanding tissues. Notably, the intrafollicular
78 microenvironment remains non-vascularized, necessitating *de novo* angiogenesis for
79 efficient substance delivery to luteal cells [27-29]. Paradoxically, vascularization in the
80 developing CL lags behind the increase in progesterone production. This temporal
81 uncoupling of metabolic demand and vascularization creates a transient avascular phase

82 during early luteogenesis, presenting a physiological enigma, i.e., how does the
83 avascular CL meet its high energetic requirements for elevated progesterone production.
84 This investigation reports a novel cellular adaptive mechanism, GC energy storage
85 (GCES), which addresses this enigma. By using single-cell/spatial transcriptomics,
86 targeted metabolic flux tracing, isotope tracing, and conditional gene silencing, we
87 show that upon luteinization initiation, GCs undergo a coordinated metabolic shift:
88 dampening overall metabolism to reduce energy expenditure coincides with the
89 strategic redirection of absorbed glucose toward glycogenesis, establishing a glycogen
90 storage pool. During the avascular phase, the luteinizing GCs use the stored glycogen
91 to satisfy the energy demanding of elevated progesterone synthesis, thereby ensuring
92 normal luteogenesis. GCES is evolutionarily conserved across species. Disrupting
93 GCES or glycogenolysis precipitate luteal insufficiency, while enhancing GCES
94 improves luteal function and fertility outcomes in mammals.

95 **RESULTS**

96 **1. Integrated multi-omics analysis reveals systemic metabolic downregulation GCs**
97 **during early luteinization**

98 To investigate the cellular response of GCs during the early stage of luteinization, the
99 mouse ovaries harvested at 0, 1 and 6 hours post-hCG (H0, H1 and H6) administration
100 were subjected to single-cell RNA sequencing to capture high-resolution
101 transcriptomes of ovarian cell populations (Figure S1A, B). Complementary spatial
102 transcriptomic analysis of publicly available mouse ovarian datasets [30] enabled
103 construction of a spatially informed transcriptomic atlas of GCs across early
104 luteinization (Figure S1C). By integrating the single-cell and spatial transcriptomic data
105 (Figure 1A; see Materials and Methods), we reconstructed a high-resolution and
106 spatially informed transcriptional atlas of GCs in pre-ovulatory follicles following
107 luteinization initiation (Figure 1B; Table S1). Principal component analysis (PCA)
108 revealed significant transcriptional divergence in GCs across timepoints (Figure 1C),

with integrated data demonstrating acceptable quality (gene training scores: ~0.8; AUC: 0.63–0.70) and enhanced resolution versus original spatial data (Figure 1D-F; S1D).

Differential expression analysis identified 3000 significantly upregulated and 3187 downregulated genes in GCs following luteinization initiation. Gene Ontology (GO) analysis demonstrated that the upregulated genes predominately enriched in established luteinization-associated processes, including *Cell Migration*, *Angiogenesis*, *Cell Adhesion*, *Extracellular Matrix Organization*, *Inflammatory Response* and *etc*, aligning with the observations of previous studies, however, two processes–*Response to Insulin* and *Glucose Homeostasis*–were newly identified (Figure 1G).

Interestingly, downregulated genes exhibited striking enrichment in diverse yet interconnected biological processes: *Mitochondrial ATP Synthesis*, *Respiratory Chain Complex I Assembly*, *Aerobic Respiration*, *Tricarboxylic Acid (TCA) Cycle*, *Respiratory Electron Transport Chain*, *Electron Transport, NADH to Ubiquinone*, *Lipid Metabolic Process*, *Fatty Acid Metabolic Process*, *Vesicle transport, ER to Golgi*, *Response to ER Stress*, *Protein Folding*, *Vesicle Transport, Golgi to ER*, *Protein N-glycan Processing*, *Protein Heterodimerization*, *ER Unfolded Protein Response*, *Protein Glycosylation*, *Oligosaccharide Biosynthesis*, *Golgi Organization*, *Protein O-linked Mannosylation*, *Protein Localization*, *Lysosomal Membrane* (Figure 1H). These processes collectively implicate a metabolic reprogramming toward quiescence, characterized by suppressed ATP-generating activities in mitochondria and energy-demanding activities in the endomembrane system. This transcriptional shift provides preliminary evidence suggesting a hitherto unrecognized cellular adaptation wherein GCs adopt energy-conserving strategies during early luteinization, suppressing ATP-generating and energy-consuming processes.

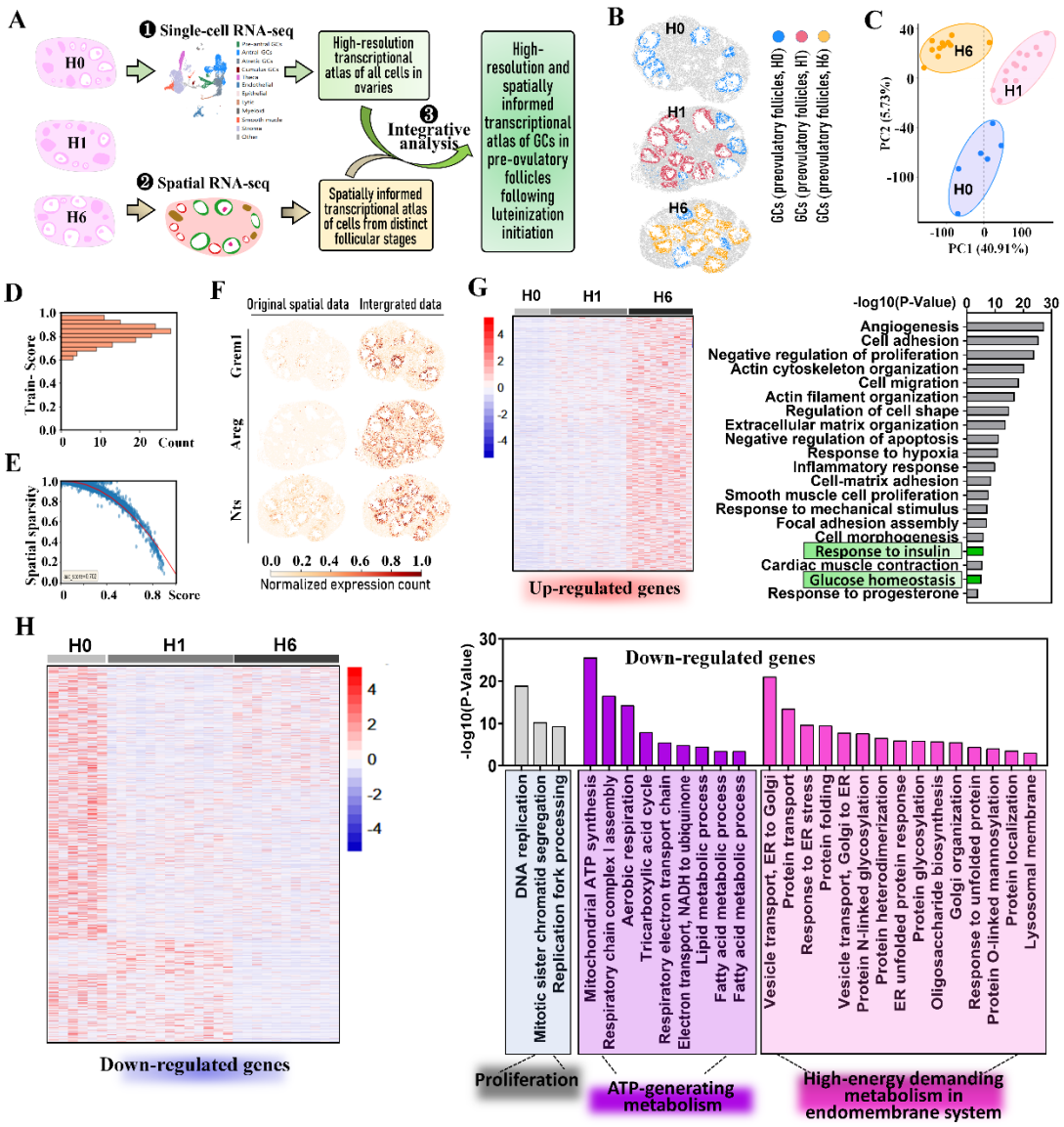

Figure 1. Integrated multi-omics analysis reveals systemic metabolic downregulation GCs during early luteinization. (A) Workflow for integrative analysis of single-cell and spatial transcriptomics data. (B) Identification of GCs in pre-ovulatory follicles at specified time points post-hCG administration using integrated analysis. (C) PCA analysis of transcriptomic differences in GCs from pre-ovulatory follicles. (D) Histogram of gene similarity scores derived from model training data. (E) Scatter plot of tangram-predicted gene scores (x-axis) versus spatial sparsity (y-axis) based on integrated transcriptome data. (F) Expression analysis of randomly selected genes demonstrated enhanced spatial resolution and clearer localization patterns in the integrated dataset compared to the original spatial transcriptomics data. (G) GO enrichment analysis of the upregulated expression cluster. Left: Heatmap of cluster-specific genes; Right: Enriched GO terms. (H) GO enrichment analysis of the downregulated expression cluster. Left: Heatmap of cluster-specific genes; Right: Enriched GO terms.

2. Metabolic attenuation and bioenergetic repression in GCs characterize early luteinization

The transcriptomic predictions of bioenergetic suppression were corroborated through multimodal analyses, including ^{13}C-glucose tracing, ultrastructural imaging, and bioenergetic profiling. Metabolic flux analysis demonstrated diminished ^{13}C-glucose

151 labeling in glycolysis and TCA cycle intermediates following hCG administration
152 (Figure 2A, B; S2A). Ultrastructural remodeling of mitochondria was evident,
153 transitioning from rounded at H0 to elongated morphologies at H6, concomitant with
154 significant reduction in ER-mitochondrial contact sites–critical platforms for metabolic
155 crosstalk (Figure 2C) [31]. This architectural reorganization paralleled profound
156 bioenergetic suppression, characterized by a 27.0% decline in mitochondrial membrane
157 potential (MMP), a 2.90-fold increase in NAD^+/NADH ratio, and a 44.1% decrease in
158 ATP synthesis relative to H0 controls (Figure 2D-F).

159 We next validated the attenuation of metabolic activity within the endomembrane
160 system through quantitative assessment of protein glycosylation, vesicular trafficking,
161 secretory capacity, and lysosomal biogenesis. Ultrastructural examination revealed that
162 GCs at H0 exhibited dilated endoplasmic reticulum (ER) cisternae and accumulated
163 transport vesicles adjacent to Golgi apparatus. By 6 hours post-hCG, ER tubules had
164 transformed into elongated cord-like structures, concurrent with a substantial reduction
165 in peri-Golgi vesicular density (Figure 2G). This morphological remodeling correlated
166 with the coordinated downregulation of genes regulating N-linked glycosylation,
167 oligosaccharide biosynthesis, vesicle assembly, and Golgi-specific O-glycosylation
168 (Figure S2B-D). Metabolomic profiling further indicated a general decline in
169 intermediates of the glycosylphosphatidylinositol (GPI) anchor biosynthesis pathway–
170 critical for glycosylation–in H6 GCs (Figure 2H), a finding corroborated by lectin
171 binding assays demonstrating significantly reduced abundance of glycosylated proteins
172 post-hCG (Figure 2I; S2E). Quantitative assessment of secretory capacity via secreted
173 alkaline phosphatase (SEAP) reporter transfection demonstrated a significant reduction
174 in SEAP activity post-hCG (Figure 2J, K; S2F). Furthermore, genes in the mannose-6-
175 phosphate (M6P) pathway—essential for lysosomal biogenesis—were significantly
176 downregulated post-hCG (Figure 2L), aligning with reduced LysoTracker Green
177 fluorescence intensity (Figure 2M) and decreased lysosomal acid phosphatase activity
178 (Figure 2N).

179 These data demonstrate metabolic quiescence transition in GCs during early
180 luteinization, validating the omics predictions.

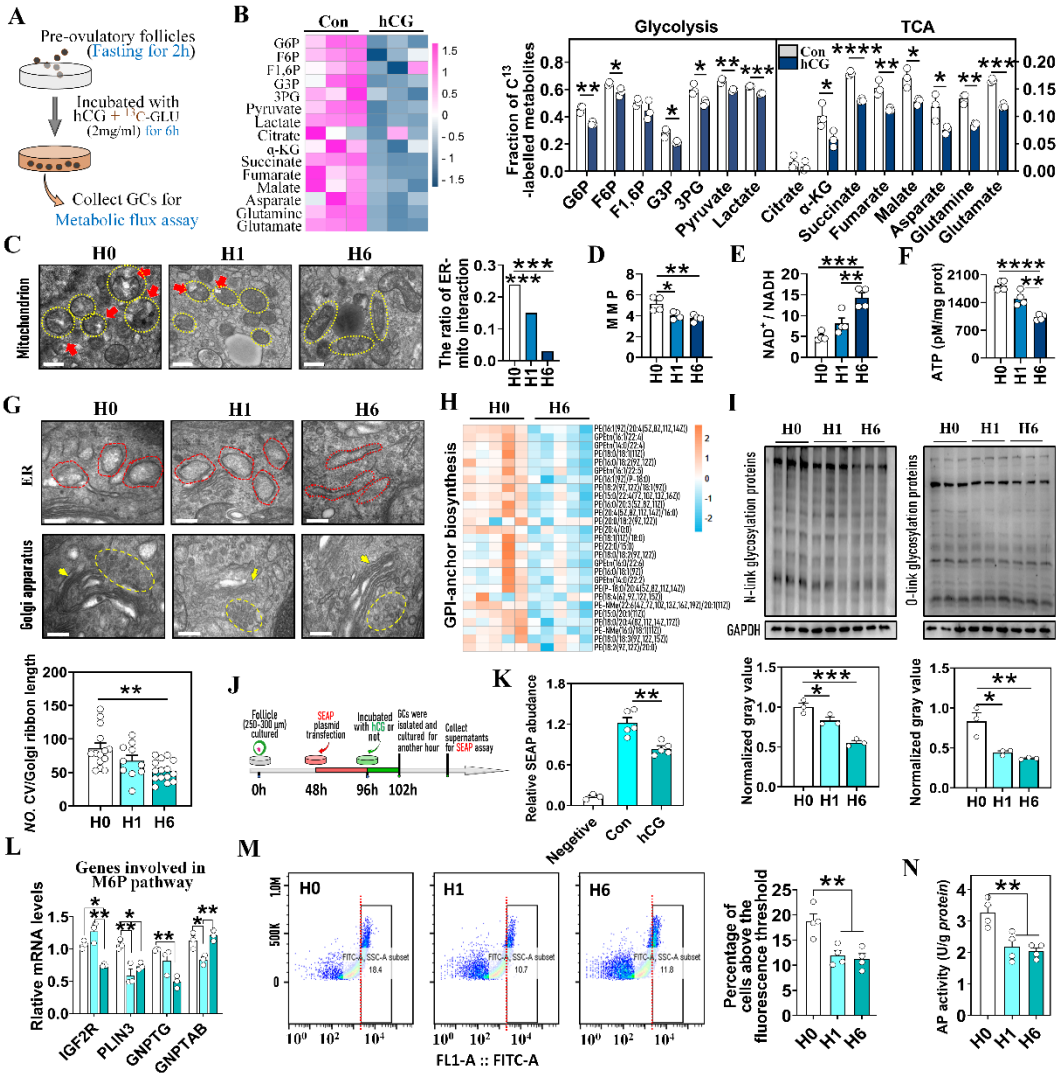

Figure 2. Metabolic attenuation and bioenergetic repression in GCs characterize early luteinization. (A) Workflow for metabolic flux analysis. Pre-ovulatory follicles were fasted for 2 hours, then cultured in luteinization medium with U-^{13}C6-glucose as sole carbon source for 6 hours before GC isolation and targeted metabolomics. (B) Quantitative analysis of ^{13}C-labeled glycolytic and TCA cycle intermediates. Left: heatmap; Right: quantification (n = 3 GC samples). The control was defined as the group cultured in hCG-free medium. (C) Changes in mitochondrial ultrastructure and ER-mitochondria contact sites following hCG injection. Left: representative images. Right: quantification. Yellow outlines: mitochondria; red arrow: contact sites. Scale bar = 500 nm. (D) MMP measured by JC-1 staining (n = 4 GC samples). (E) NAD$^+$/NADH ratio determined by colorimetric assay (n = 4 GC samples). (F) ATP levels measured by luciferase bioluminescence assay (n = 4 GC samples). (G) Ultrastructural changes in ER and Golgi apparatus in GCs following hCG injection. Top: representative images. Down: quantification. Red outlines: ER; yellow arrow: Golgi apparatus; yellow outline: transport vesicles. Scale bar = 200 nm. (H) Heatmap showing changes in the content of GPI-anchor biosynthesis pathway intermediates post-hCG (n = 5 GC samples). (I) Quantification of N-linked (Stained by Concanavalin A)/O-linked glycoprotein (Stained by Peanut Agglutinin) abundance in GCs by lectin blotting. Top: lectin blot; Down: quantification (n = 3 GC samples). (J) Workflow for SEAP reporter assay. (K) Quantification of SEAP secreted into the supernatant using chemiluminescence assay (n = 5 supernatant samples). (L) Changes in M6P pathway gene expression post-hCG injection (n = 3 GC samples). (M) Flow cytometry analysis of GCs with high-intensity Lyso-tracker green fluorescence. Red line: fluorescence intensity threshold; cells right of threshold line classified as high-intensity fluorescent (n = 4 GC samples). (N) Detection of changes in lysosomal acid phosphatase activity using colorimetric

assay (n = 4 GC samples). Data represent mean ± SD. Significance determined by two-tailed unpaired Student's t-test (G) and one-way ANOVA followed by Tukey's post hoc test (*P<0.05, **P<0.01, ***P<0.001, ****P<0.0001). Results shown (C-G, I-N) are from one of at least three independent replicates; all experiments produced comparable data.

3. Enhanced glucose uptake supports glycogen biosynthesis in GCs during early luteinization

Intriguingly, despite transitioning to a metabolically quiescent state, GCs at H6 exhibited a significant increase in glucose uptake compared to H0 controls (Figure 3A). Transporter expression profiling identified SLC2A1 as the predominant glucose transporter of this enhanced uptake (Figure 3B; S3A). Intracellular glucose can be directed toward ATP generation or storage as lipids or glycogen (Figure 3C) [32]. Metabolic flux analysis ruled out significant catabolic utilization (Figure 2A, B), and nor for the lipid storage since colorimetric assays revealed the reduced intracellular free fatty acids and triglycerides (Figure S3B, C). To directly assess glycogen conversion, we performed ^{13}C-glucose tracing coupled with Liquid Chromatograph-Tandem Mass Spectrometer (LC-MS/MS). hCG-treated GCs exhibited pronounced ^{13}C enrichment in glycogen (35% incorporation versus, 8% in controls; Figure 3D, E), demonstrating preferential glycogen biosynthesis. Consistent with this, Western blotting and qRT-PCR analysis detected activation of the glycogenesis pathway following hCG administration (Figure 3F; S3D). Complementary Periodic Acid-Schiff (PAS) staining and colorimetric quantification confirmed a significant elevation in glycogen content within H6 GCs (Figure 3G, H).

We next characterized the temporal dynamics of glycogen storage and its functional correlates throughout luteinization process. Integrated analysis defined distinct phases: a glycogenesis phase (H0-H9) followed by a glycogenolysis phase (H9-H15), evidenced by glycogenesis/glycogenolysis pathway protein expression (Figure 3I) and PAS staining (Figure 3J). Notably, during glycogenesis phase, ATP production declined (Figure 3K) while progesterone levels rose gradually up to 80 ng/g (Figure 3L). Upon entering glycogenolysis phase (H9-H15), ATP levels surged (Figure 3K) coincident with the peak progesterone secretion (~200 ng/g; Figure 3L). Critically, this glycogenolysis phase–characterized by high energy demand for steroidogenesis–occurred within the developing CLs prior to the establishment of internal vascularization (Figure 3M).

These data demonstrate that during the early luteinization phase, GCs undergo a coordinated metabolic shift: dampening overall metabolism to reduce energy expenditure coincides with the strategic redirection of absorbed glucose toward

glycogenesis, establishing a glycogen storage pool. We postulate that this preformed glycogen serves as a critical energy reservoir for the avascular CL.

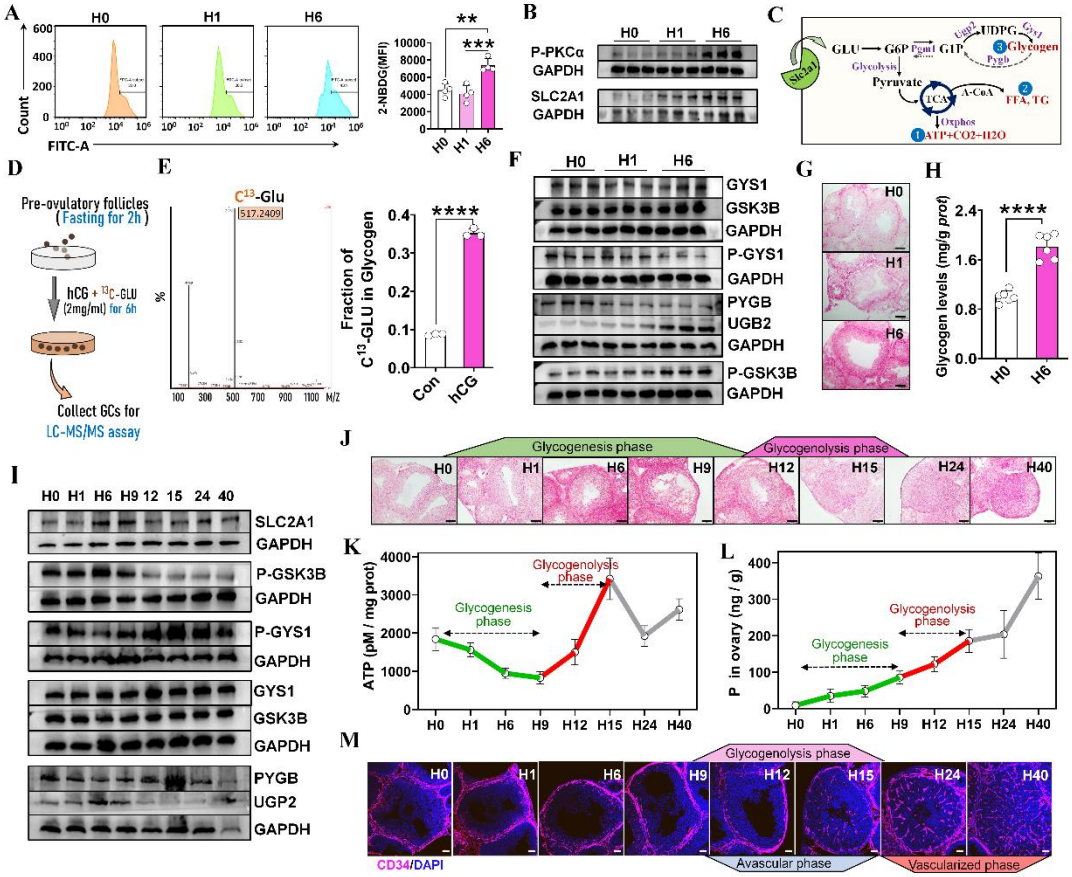

Figure 3. Enhanced glucose uptake supports glycogen biosynthesis in GCs during early luteinization. (A) Flow cytometric analysis of cellular glucose uptake capacity post-hCG injection. Isolated GCs were incubated with fluorescent analog 2-NBDG (100 μM) for 30 minutes prior to analysis. Left: representative images; Right: quantification (n = 4 GC samples). (B) Western blotting analysis of SLC2A1 and its upstream kinase P-PKCα in GCs post-hCG injection (n = 3 GC samples). (C) Schematic of intracellular glucose carbon flux. (D) ^{13}C-glucose tracing workflow. Pre-ovulatory follicles fasted 2 hours, then cultured in luteinization medium with U-^{13}C6-glucose (sole carbon source) for 6 hours before GC isolation and LC-MS/MS analysis. (E) Quantitative ^{13}C enrichment in glycogen (n = 3 GC samples). The control was defined as the group cultured in hCG-free medium. (F) Changes in glycogenesis/glycogenolysis proteins during early luteinization (n = 3 GC samples). (G) PAS staining of glycogen in GCs during early luteinization. Scale bar = 100 μm. (H) Colorimetric quantification of glycogen content (n = 6 GC samples). (I) Changes in glycogenesis/glycogenolysis proteins throughout luteinization. (J) PAS staining of glycogen throughout luteinization. Scale bar = 100 μm. (K) ATP content changes throughout luteinization (n = 5-6 GC samples). (L) Radioimmunoassay of progesterone in ovarian homogenates throughout luteinization (n = 4-7 ovarian samples). (M) Vascularization changes assessed by CD34^{+} endothelial cells (red) during luteinization. Nuclei counterstained with DAPI (blue). Scale bar = 50 μm. Data represent mean ± SD. Significance determined by one-way ANOVA with Tukey's post hoc test (A, K, L) or two-tailed unpaired Student's t-test (E, H) (*P < 0.05, **P < 0.01, ***P < 0.001, ****P < 0.0001). Results shown are from one of at least three independent replicates; all experiments produced comparable data.

264 **4. Mobilization of glycogen storage to fuel luteal steroidogenesis during the**
265 **avascular phase**
266 To test whether the stored glycogen in GCs is used to fuel the avascular CL for
267 steroidogenesis, we augmented glycogen storage during glycogenesis phase via 2g/kg
268 dose of glucose (glucose tolerance dose) administration (Figure 4A-C). By 15 hours
269 post-hCG (H15), the glucose-loaded luteinizing GCs exhibited reduced NAD^+/NADH
270 ratio, increased ATP generation, upregulated luteal gene expression and increased
271 progesterone secretion compared to the controls (Figure 4D, E; S4A). This functional
272 enhancement persisted until H40 (Figure S4B), indicating the glycogen storage as a
273 critical determinant of luteal function.
274 To further validate the functional importance of glycogen, RNA interference was
275 performed to suppress the glycogen synthesis. *In vitro* knockdown of glycogenesis genes
276 *Ugp2* and *Gys1* did not impair follicular development and ovulation but markedly reduced
277 GC glycogen storage in pre-ovulatory follicles (Figure 4F, G; S5A-C). This intervention
278 precipitated a profound bioenergetic crisis at H15, characterized by increased
279 NAD^+/NADH ratio, diminished MMP, reduced ATP generation, significantly suppressed
280 progesterone synthesis and luteal gene expression (Figure 4H-J; S5D, E). *In vivo* ovarian
281 bursa delivery of *Ugp2* and *Gys1* interference plasmids (Figure 4K-M; S6A) recapitulated
282 this bioenergetic crisis with: increased NAD^+/NADH, decreased ATP, downregulated
283 luteal gene expression and reduced serum progesterone (Figure 4N-P; S6B).
284 Complementarily, inhibition of glycogen catabolism during the glycogenolysis phase
285 using the PYGB inhibitor–Ingliforib (Figure 4Q, R) also induced luteal insufficiency,
286 evidenced by decreased ATP production, downregulated luteal gene expression and
287 attenuated progesterone synthesis in the glycogen-constrained luteinizing GCs (Figure
288 4S, T; S6C).
289 To definitively investigate the functional necessity of glycogen storage *in vivo*, the
290 GC-specific *Gys1* conditional knockout mice (cKO-*Gys1*) were generated using a
291 Gyp19a1-Cre driver system (Figure 4U; S6D). This genetic ablation abolished glycogen
292 accumulation within GCs of the mice (Figure 4V). Concomitantly, cKO mice exhibited
293 significant bioenergetic perturbation in their avascular CLs, including elevated
294 NAD^+/NADH ratio, impaired ATP production and significantly suppressed progesterone
295 synthesis along with attenuated luteal gene expression at H15 (Figure 4W, X; S6E).
296 Moreover, cKO mice displayed a significant decrease in litter size compared to
297 $Gys1^{floxp/floxp}$ (Figure 4Y).

These data confirm that glycogenesis in GCs establishes an essential energy reservoir, which mobilized during the avascular phase to fuel the bioenergetic demands of progesterone production in nascent CL. This cellular adaptive mechanism hereafter termed GCES.

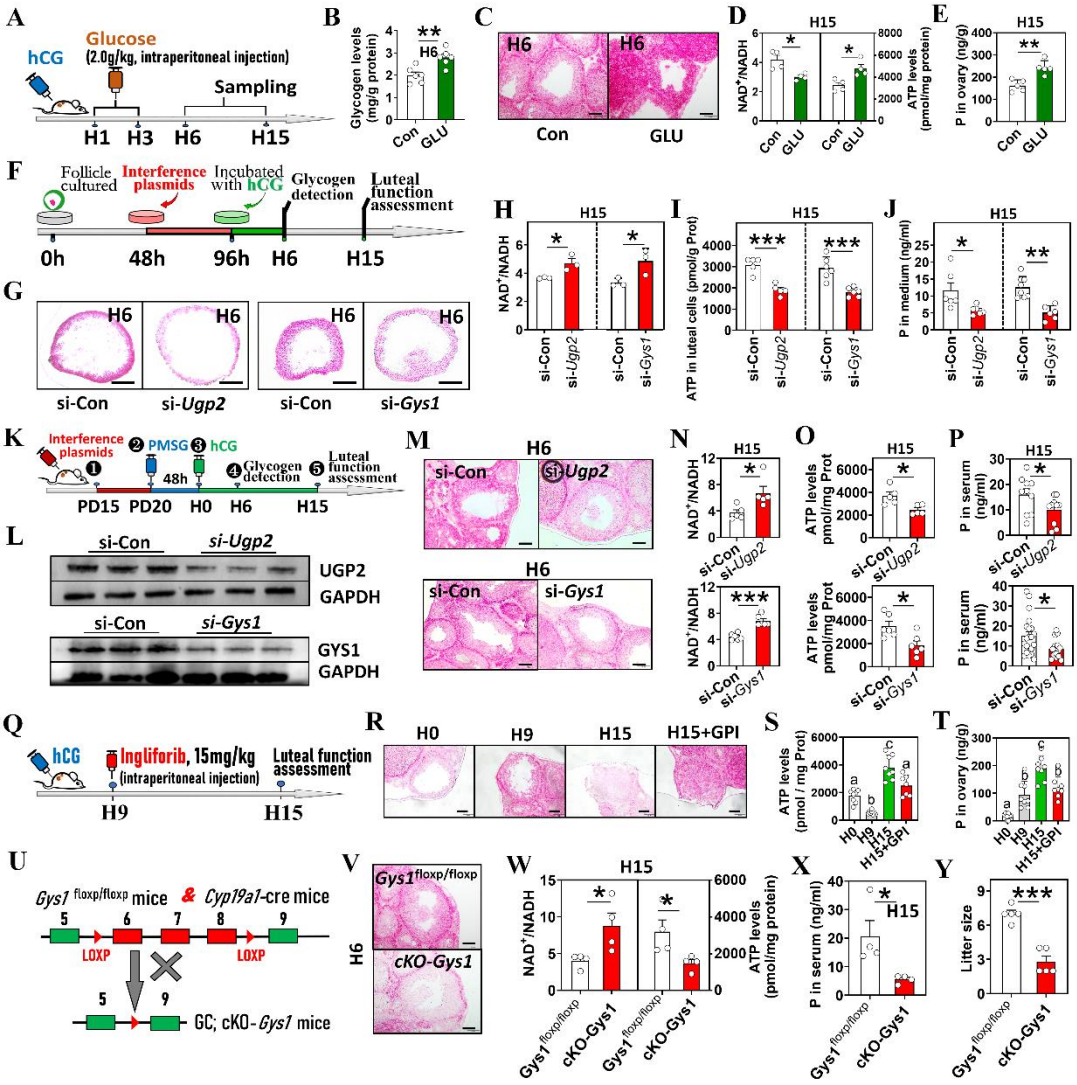

Figure 4. Mobilization of glycogen storage to fuel luteal steroidogenesis during the avascular phase. (A) Experimental design for panels (B-E). (B) Colorimetric quantification of glycogen content in GC post-glucose injection (n = 6 GC samples). (C) PAS staining of glycogen storage post-glucose injection; scale bar = 100 µm. (D) Alterations in NAD^+/NADH ratio and ATP contents post-glucose injection (n = 4 GC samples). (E) Progesterone levels in ovarian homogenates measured by radioimmunoassay post-glucose injection (n = 5 ovarian samples). (F) Experimental design for *Ugp2*/*Gys1* knockdown in cultured mouse follicles. Luteinizing GCs isolated at H15 for functional assessment. (G) Changes in GC glycogen storage post-*Ugp2* and *Gys1* knockdown. The commercial scrambled siRNA serving as si-Control (si-Con). Scale bar = 100 µm. (H) Alterations in NAD^+/NADH in GCs post-knockdown; n = 3 GC samples. (I) ATP content in GCs post-knockdown (n = 5-6 GC samples). (J) Progesterone in culture medium post-knockdown (n = 6-8 samples). (K) Experimental design for in vivo lentiviral-mediated *Ugp2*/*Gys1* knockdown. Luteinizing GCs isolated from CLs at H15 for functional assessment. (L) Western blotting confirmation of *Ugp2*/*Gys1* knockdown in ovaries (n = 3 ovarian samples). (M) PAS staining of glycogen storage post-knockdown. Scale bar = 100 µm. (N) NAD^+/NADH alterations in GCs post-knockdown (n = 5-6 GC samples). (O) ATP content changes in GCs post-knockdown (n = 5-6 GC samples). (P) Progesterone level alterations post-knockdown; n = 10 (si-*Ugp2*), 15-21 (si-*Gys1*) serum samples. (Q) Experimental design for Ingliforib treatment in vivo. (R) PAS staining validation of Ingliforib-

321 mediated glycogenolysis inhibition. Scale bar = 100 μm. (S) ATP levels in luteinizing GCs post-
322 Ingliforib treatment (n = 7-8 GC samples). (T) Progesterone in ovarian homogenates post-
323 Ingliforib treatment (n = 8 ovarian samples). (U) Schematic representation of the conditional
324 knockout of *Gys1* in mouse GCs. (V) PAS staining of glycogen storage in GCs post-knockout.
325 Scale bar = 100 μm. (W) Alterations in NAD^+/NADH ratio and ATP contents (n = 4 GC
326 samples). (X) Progesterone level alterations post-knockout (n = 4 serum samples). (Y) Litter
327 size alterations post-knockout (n = 5 mice). Data represent mean ± SD. Significance determined
328 by two-tailed unpaired Student's t-test or one-way ANOVA with Tukey's post hoc test (S, T)
329 (*P < 0.05, **P < 0.01, ***P < 0.001). Results shown are from one of twice (V-Y) or at least
330 three (A-T) independent replicates; all experiments produced comparable data.

331 **5. hCG (LH) induces glycogen storage via MAPK-RUNX1-Insulin signaling axis**

332 To identify the intracellular signaling regulating GCES, KEGG enrichment analysis
333 was performed. The results showed a significant induction of insulin signaling during
334 early luteinization (Figure 5A). Consistent with this, qRT-PCR and Western blotting
335 demonstrated that hCG injection markedly increased both mRNA and protein levels of
336 insulin/IGF-1 receptors (INSR and IGF1R) in GCs, concomitant with enhanced
337 receptor phosphorylation (Figure 5B; S7A). Functional validation demonstrated that
338 insulin alone was sufficient to enhance glucose uptake and glycogen storage in GCs.
339 Conversely, pharmacological inhibition of INSR/IGF1R with BMS536924 abolished
340 hCG-induced glucose uptake and glycogen storage (Figure 5C-F), confirming the
341 necessity of insulin signaling for hCG-driven glycogen storage.

342 We next investigated mechanism by which hCG (LH) initiates insulin signaling. In
343 addition to insulin signaling, the significant induction of the MAPK (ERK1/2) signaling
344 during early luteinization was also observed with KEGG analysis (Figure 5A). Among the
345 transcription factors potently induced by hCG, RUNX1–a known downstream target of
346 MAPK–was ranked relatively higher (Figure 5G, H). Moreover, publicly available ChIP-seq
347 data [23] indicated specific binding of RUNX1 to *Igf1r* and *Insr* promoters (Figure 5I). Taken
348 together, these data collectively suggest that hCG activates insulin signaling and glycogenesis
349 via the MAPK-RUNX1 cascade. To test this, the C16-PAF was used to active MAPK
350 signaling. This treatment recapitulated the effects of hCG supplementation including
351 RUNX1 upregulation, insulin signaling activation and glycogen storage in GCs. Conversely,
352 MAPK inhibition with U0126 abolished all these effects induced by hCG (Figure 5J, K).
353 Furthermore, RUNX1 knockdown in cultured follicles suppressed hCG-induced insulin
354 signaling activation and glycogen storage in GCs (Figures 5L-M; S7B).

355 Finally, to identify whether there is a direct transcriptional regulation between
356 RUNX1 and insulin/IGF-1 receptors, both electrophoretic mobility shift assays (EMSA)
357 and chromatin immunoprecipitation quantitative PCR (ChIP-qPCR) were performed.

EMSA confirmed the specific RUNX1 binding sites with the predicted consensus motifs within the *Igf1r* and *Insr* promoters (Figure 5O; S7C-E). ChIP-qPCR confirmed an increased RUNX1 occupancy at these promoter regions at H6 (Figure 5P). Site-directed mutagenesis localized the RUNX1 response element to the TGTGGT motif in both promoters (Figures 5M; S7F). These results demonstrate that hCG (LH)-MAPK-RUNX1-Insulin signaling pathway is a key regulator of GCES.

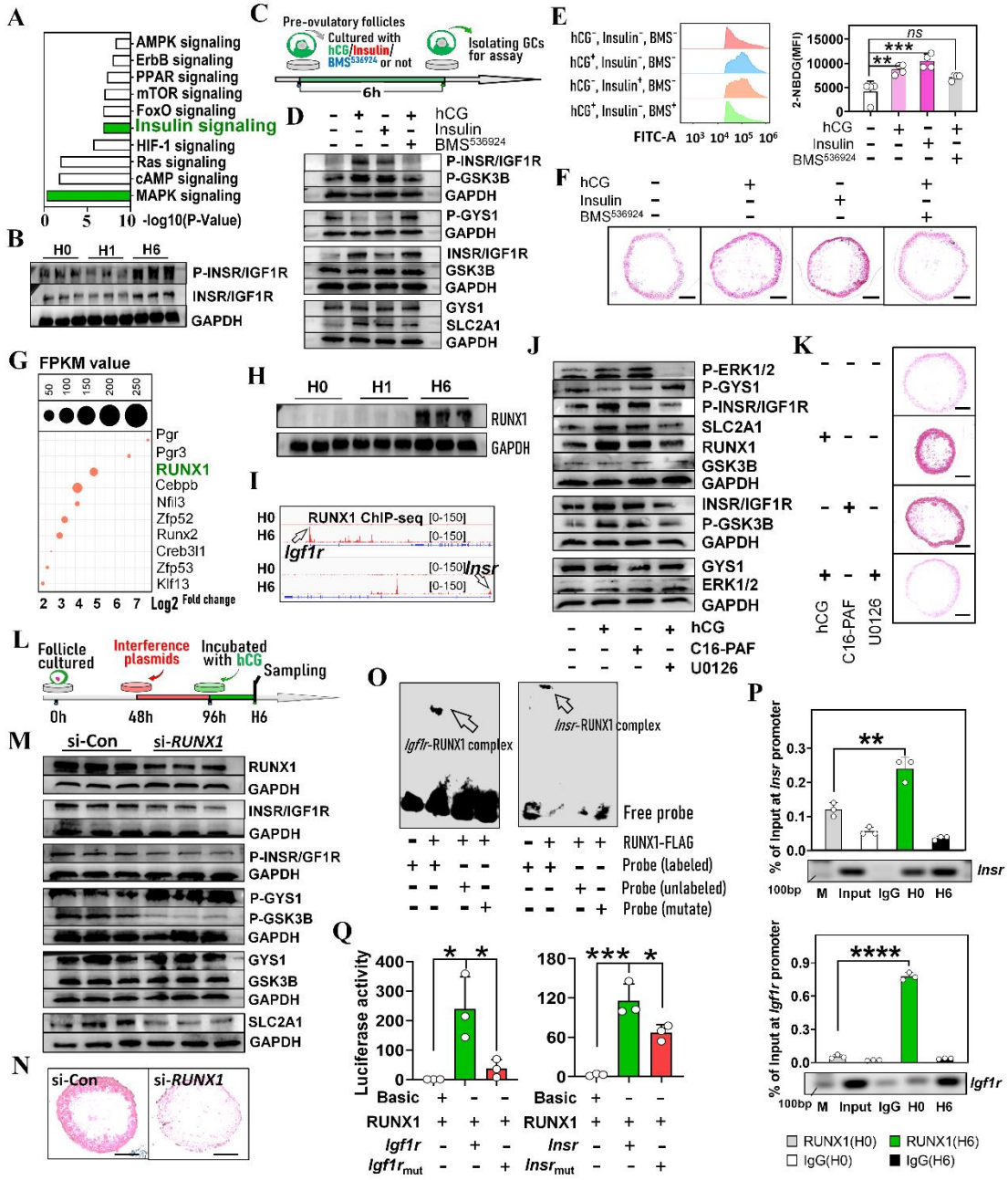

Figure 5. hCG (LH) induces glycogen storage via MAPK-RUNX1-Insulin signaling axis. (A) KEGG pathway analysis of signaling activation in GCs post-hCG injection. (B) Western blotting analysis of INSR/IGF1R activity in GCs post-hCG injection (n = 3 GC samples). (C) Experimental design for panels (D-F). (D) Western blotting analysis of glycogenesis related proteins in GCs after insulin pathway modulation. (E) Flow cytometric analysis of glucose

uptake capacity in GCs. Left: representative images; Right: quantification. Isolated GCs were incubated with fluorescent analog 2-NBDG for 30 minutes prior to analysis (n = 4 GC samples). (F) PAS staining of glycogen stores in GCs after insulin signaling manipulation. Scale bar = 100 μm. (G) Top 10 transcription factors upregulated in GCs by hCG (bubble plot). (H) Western blotting analysis of RUNX1 expression in GCs post-hCG injection (n = 3 GC samples). (I) ChIP-seq profiles of RUNX1 binding at *Igf1r* and *Insr* promoters. Arrows: enrichment peaks. (J) Western blotting analysis of RUNX1 and glycogenesis related proteins in GCs after MAPK pathway modulation. (K) PAS staining of glycogen stores after MAPK pathway modulation. Scale bar = 100 μm. (L) Experimental design for panels (M, N). (M) Western blotting analysis of glycogenesis regulators in GCs post-RUNX1 knockdown (n = 3 GC samples). (N) PAS staining of glycogen stores after RUNX1 knockdown. Scale bar = 100 μm. (O) EMSA validating RUNX1 binding to *Igf1r* and *Insr* promoter motifs. (P) ChIP-qPCR quantification of RUNX1 binding to *Igf1r* and *Insr* promoters (n = 3 GC samples). (Q) Dual-luciferase reporter assays identifying RUNX1-responsive elements in *Igf1r* and *Insr* promoters (n = 3 cellular samples). Data represent mean ± SD. Significance determined by one-way ANOVA with Tukey's post hoc test (*P < 0.05, **P < 0.01, ***P < 0.001, ****P < 0.0001). Results shown (B-F, H, J-Q) are from one of at least three independent replicates; all experiments produced comparable data.

6. GCES augmentation enhanced luteal function and pregnancy outcomes in mouse and ovine models

To assess the clinical relevance of GCES, glycogen storage in mouse GCs was augmented with timely glucose administration (Figures 6A, B). This intervention significantly elevated progesterone levels by gestation day 15 (GD15; Figure 6C). Crucially, the progesterone-enhancing effect of glucose administration was contingent exclusively into the glycogenesis phase; glucose administration outside this temporal window was proved no effective (Figure S8A). Compared to controls, the glucose-treated mice exhibited a reduced fetal regression rate (Figure 6D), increased fetal and placental weights (Figure 6E), although fetal number remained unchanged (Figure 6D). To critically evaluate the functional relevance to assisted reproduction, we further assessed the impact of glucose administration on the farrowing rate following embryo transfer (Figure 6F). Glucose treatment during the temporal window significantly increased the farrowing rate compared to the control group (Figure 6G), demonstrating its potential utility in reproductive technologies.

The functional conservation of GCES was also investigated in sheep, a mono-ovulatory species. Similar to the mouse model, LH injection significantly upregulated the expression of genes involved in insulin and glycogenesis pathway, reduced ATP generation and increased glycogen accumulation in sheep GCs (Figures 6H, I; S8B, C).

The subsequent glucose potentiation (1.5g/kg, aligned with human glucose tolerance dose) further increased glycogen storage (Figures 6I, J), concomitantly elevating progesterone levels and luteal gene expression by GD20 (Figure 6K; S8D). Strikingly, the pregnancy rate was significantly higher in the glycogen-augmented group (81.25%) compared to controls (63.45%; $p < 0.01$, Figure 6L).

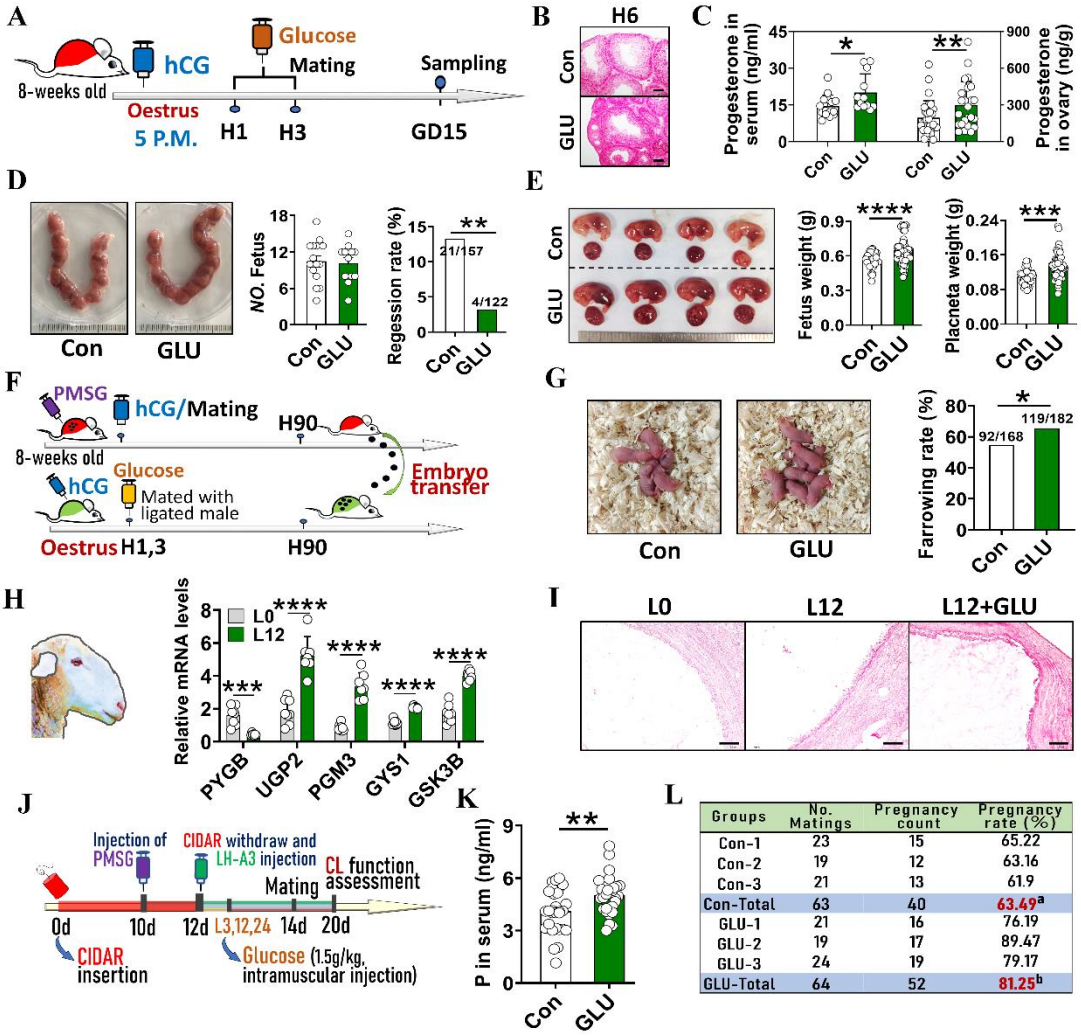

Groups	No. Matings	Pregnancy count	Pregnancy rate (%)
Con-1	23	15	65.22
Con-2	19	12	63.16
Con-3	21	13	61.9
Con-Total	63	40	63.49[a]
GLU-1	21	16	76.19
GLU-2	19	17	89.47
GLU-3	24	19	79.17
GLU-Total	64	52	81.25[b]

Figure 6. GCES augmentation enhanced luteal function and pregnancy outcomes in mouse and ovine models. (A) Experimental design for panels B to E. (B) PAS staining of glycogen. Scale bar = 100 μm. (C) Effects of glucose intake on serum and ovarian progesterone levels at GD15; n (serum) = 15 (Con), 12 (GLU); n (ovarian homogenate) = 30 (Con), 24 (GLU). (D) Effects of glucose intake on fetal number and regression rates at GD15 (n = 15 pregnant mice). (E) Effects of glucose intake on fetal and placental weights at GD15; n = 4 (Con) and 5 (GLU) pregnant mice. (F) Embryo transfer experimental schematic. (G) Effects of glucose intake on the farrowing rate of transferred embryos. (H) qRT-PCR analysis of glycogen metabolism genes in ovine GCs pre-(L0) and 12 hours post-LH injection (L12); n = 8 (L0), 7 (L12) GC samples. (I) PAS staining of glycogen in ovine GCs post-LH injection. Scale bar = 500 μm. (J) Experimental design for panels I to L. (K) Effects of glucose intake on serum progesterone levels (n = 30 serum samples). (L) Effects of glucose intake on sheep pregnancy rate after breeding. Data represent mean ± SD. Significance determined by two-tailed unpaired

426 Student's t-test or chi-square test (D, G and L) (*P < 0.05, **P < 0.01, ***P < 0.001, ****P <
427 0.0001). Results shown are from one of at least three independent replicates; all experiments
428 produced comparable data.

429 **7. Timely oral glucose administration enhances GCES and luteal function in**
430 **humans**

431 Transitioning to humans, the transcriptome of human GCs following hCG
432 administration was analyzed by using public databases [33]. GO analysis revealed the
433 enrichment of these hCG-downregulated genes in high-energy-demanding processes
434 and ATP production, similar to the findings in mouse and ovine models (Figure 7A).
435 Moreover, the expression of glucose transporters *SLC2A13*, *SLC2A14* and *SLC2A3*
436 exhibited a sharp increase at H12, returning to baseline by H32 (Figure 7B).
437 Furthermore, hCG administration significantly upregulated insulin signaling
438 components, including *IGF1R*, *IGFBP1*, *IGFBP3*, *IGFBP5* and *IRS2* (Figure 7C),
439 supporting the evolutionary conservation of GCES mechanisms in humans.

440 To translate these findings clinically, we recruited volunteers undergoing assisted
441 reproductive technology (ART). Participants were instructed orally intake of 75g
442 glucose (glucose tolerance dose) at 12 hours post-hCG trigger. Their progesterone
443 synthetic capacity was assessed 24 hours post-glucose ingestion (Figure 7D). This
444 timely oral glucose administration significantly augmented glycogen storage within
445 human GCs (Figure 7E). Compared to the control group, the glucose-treated group
446 demonstrated significantly upregulated expression of luteal genes in luteinizing GCs
447 (Figure 7F), culminating in a ~73% increase ($p < 0.001$) in mean progesterone
448 concentration within follicular fluid (Figure 7G).

449 These results demonstrate that a single, timely oral glucose intervention following
450 hCG trigger significantly elevates glycogen reserves in human GCs and increases
451 progesterone production.

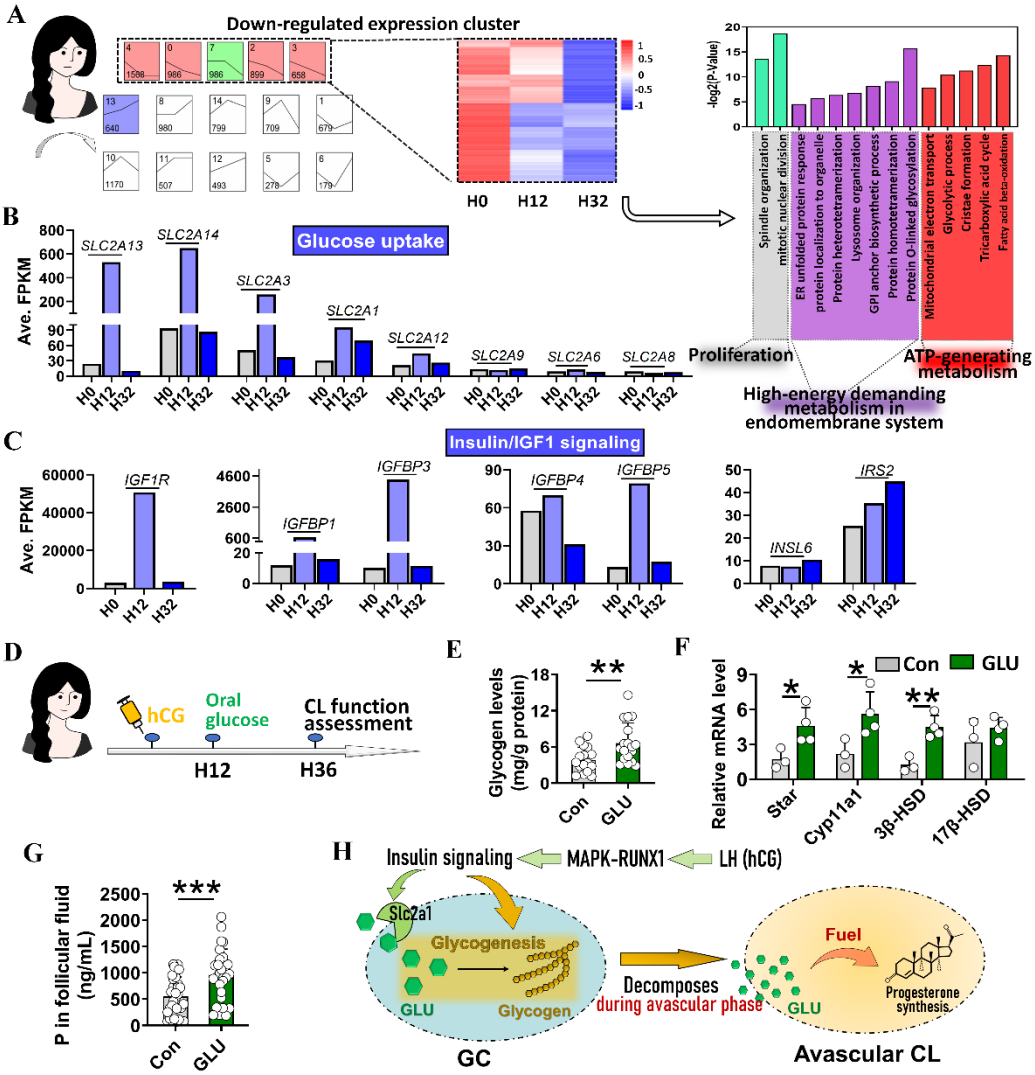

Figure 7. Timely oral glucose administration enhances GCES and luteal function in humans. (A) GO enrichment analysis of the downregulated expression cluster in human GCs post-hCG injection. Left: heatmap; Right: enriched GO terms. (B) Expression of glucose transporter genes in GCs post-hCG injection. (C) Expression of insulin pathway genes in GCs post-hCG injection. (D) Experimental design for panels E to G. Volunteers were randomly selected from women undergoing ART treatment and responding normally to controlled ovarian hyperstimulation. (E) Colorimetric qualification of glycogen storage in GCs post-glucose intake; n = 16 (Con), 18 (GLU) GC samples. (F) qRT-PCR analysis of luteal gene expression post-glucose intake; n = 3 (Con), 4 (GLU) GC samples. (G) Progesterone levels in follicular fluids measured by radioimmunoassay post-glucose intake; n = 34 (Con), 28 (GLU) samples. (H) A diagram depicting GCES. Data represent mean ± SD. Significance determined by two-tailed unpaired Student's t-test (*P < 0.05, **P < 0.01, ***P < 0.001). The experiments (E, G) were repeated twice with consistent results.

466 **DISCUSSION**

467 The acquisition of progesterone synthesis capacity precedes the vascularization in the
468 CL. How does the avascular CL meet the substantial bioenergetic demands for the high
469 level of progesterone production is still unknown. Our study resolves this enigma by
470 identifying GCES as the key mechanism. We demonstrate that during early
471 luteinization, hCG (LH) orchestrates a metabolic transition in GCs via the MAPK-
472 RUNX1-Insulin signaling axis, redirecting glucose toward glycogenesis. This
473 strategically stored glycogen is subsequently mobilized to fuel intensive progesterone
474 production throughout the avascular phase, ensuring normal luteogenesis (Figure 7H).
475 The GCES process fundamentally refines our understanding of luteinization. This
476 process strikingly parallel to oocyte nutrient provisioning for preimplantation embryos
477 [34] highlights conserved regulatory strategies in reproduction. Moreover, GCs emerge
478 as a novel insulin-sensitive glycogenic cell type, distinct from hepatocytes and
479 myocytes [35,36], with broad physiological implications.

480 GCES not only serves as an energy source for avascular CL but also profoundly
481 influencing mature luteal function (Figure S4B), indicating significant translational
482 promise. GCES enhancement improved luteal function in both polytocous (mice) and
483 monotocous (sheep) species, leading to marked increases in pregnancy rates. In human
484 trials, the timely oral glucose administration induces the GCES enhancement,
485 increasing progesterone content by ~73%. Crucially, this GCES-mediated luteal
486 support was achieved solely through glucose intake, bypassing pharmaceutical agents,
487 thereby being exceptional safety. This is particularly significant since no treatment for
488 luteal insufficiency has been reported to improve pregnancy rates in natural menstrual
489 cycle [3]. Therefore, we propose a novel preconception strategy: peri-ovulatory intake
490 of glucose or high-glycemic-index foods (such as cakes, milk tea, candies) as a potential
491 means to mitigate luteal insufficiency and improve fertility outcomes. Given its safety,
492 accessibility, ease of use and cost-effectiveness, this approach could be widely adopted
493 in populations with a higher incidence of luteal insufficiency, potentially reducing
494 reliance on conventional luteal phase support–especially in women who experience the
495 dual risk factors of early pregnancy bleeding and a history of previous miscarriages
496 [37,38].

497 In livestock production, GCES-based luteal enhancement could integrate
498 seamlessly with estrus synchronization and embryo transfer to boost pregnancy rates

499 and reduce infertility or miscarriage attributable to luteal deficiency, as validated in
500 sheep (Figure 6K, L; S8D). Importantly, optimal implementation requires precision
501 timing, dosage (the dose employed herein was glucose tolerance dose), and frequency
502 of glucose administration. Murine data identified a ≤9-hour post-hCG window (marked
503 by glucose transporter/glycogen synthase upregulation) for effective glucose
504 intervention. Extra-window supplementation fails to improve luteal function (Figure
505 S8A), necessitating species-tailored glucose regimens–a key challenge in clinical
506 translation.

507 While GCs and theca cells jointly contribute to luteogenesis, GO analysis revealed
508 a distinct metabolic divergence. Unlike GCs, theca cells neither enter metabolic quiesce
509 nor accumulate glycogen following luteinization initiation (Figure S9A-D). Thus,
510 glycogen storage represents a GC-specific adaptation. Intriguingly, theca cells exhibit
511 significantly higher glycogen content compared to other follicular cell types during
512 folliculogenesis (Figure S9E), suggesting that theca cells may also engage in glycogen
513 storage, albeit initiating this process earlier than GCs.

514 In summary, this study introduces the novel concept of GCES and demonstrates
515 that enhancing GCES via timely glucose administration improves luteal function in
516 different species including humans. These insights advance reproductive physiology
517 and hold substantial promise for developing novel therapeutic approaches to address
518 luteal insufficiency in both livestock and human.

519 **LIMITATIONS**

520 While we have identified the LH (hCG)-MAPK-RUNX1-Insulin axis regulating
521 glycogen storage in GCs, the signaling pathway(s) inducing metabolic quiescence
522 remains undefined. Beyond elevated energy demands, robust progesterone production
523 also requires substantial cholesterol precursor, yet how the developing CL maintains
524 cholesterol supply during its avascular phase has not been investigated. Furthermore, the
525 mandatory progesterone supplementation following embryo transfer in ART protocols
526 [39,40] precludes direct assessment of GCES-mediated improvement in mature CL
527 function and pregnancy outcomes of humans. Future studies should aim to: (i) delineate
528 the mechanisms governing GC metabolic quiescence and cholesterol provision, and (ii)
529 quantify the effects of GCES enhancement on human pregnancy rates in natural
530 conception cohorts.

MATERIALS AND METHODS

Experimental design

This study commenced with the prediction of GC metabolic alterations during early luteinization using multi-omics profiling. These predictions were experimentally validated, defining a novel cellular adaptive mechanism, GCES. The functional impact of GCES on luteogenesis was then investigated through targeted manipulation in vitro and in vivo. Meanwhile, the regulatory pathway controlling GCES was elucidated. Finally, the translational potential of GCES was evaluated across species and in a preliminary clinical setting.

(1) **Multi-Omics Profiling of GC Dynamics during Early Luteinization**: Integrated single-cell and spatial transcriptomics analysis was performed to delineate high-resolution transcriptional profiles of GCs within pre-ovulatory follicles at 0, 1, and 6 hours post-hCG administration, simulating the LH surge. Subsequent GO enrichment analysis of transcriptomic profiles predicted metabolic alterations in GCs during early luteinization, revealing attenuated high-energy demanding and ATP-generating activities alongside enhanced insulin responsiveness and glucose homeostasis.

(2) **Experimental Validation of Metabolic Alterations**: Next, a multi-modal approach was employed to validate the omics-derived predictions, encompassing: targeted metabolomics, electron microscopy, flow cytometry, mitochondrial functional assays, glucose uptake capacity measurements, isotopic tracing, qRT-PCR, Western blotting, immunofluorescence, PAS staining, and enzymatic activity assays. This validation confirmed that GCs enter a metabolically quiescent state while concurrently enhancing glucose uptake and conversion to glycogen for storage, *i.e.* GCES.

(3) **Functional Impact of GCES on luteinization**: To investigate whether GCES governs luteal function by modulating energy availability during the avascular phase, glycogen storage was manipulated assessed both in vitro and in vivo via: (i) glucose supplementation to enhance glycogen storage; (ii) RNA interference and conditional knockout strategies to block glycogen storage; and (iii) pharmacological inhibition of glycogen catabolism. The functional consequences

562 of these interventions on luteal energy supply and progesterone biosynthesis were
563 rigorously evaluated.
564 (4) **Validation of GCES Regulatory Pathway**: Bioinformatics-driven analyses,
565 coupled with flow cytometry, pharmacological modulation (inhibitors/activators),
566 RNA interference, Western blotting, EMSA, ChIP-qPCR, luciferase reporter assay,
567 and PAS staining, were utilized to elucidate the signaling pathway(s) governing
568 GCES.
569 (5) **Translational Evaluation of GCES in a Three-Phase Approach**: (i) The
570 conservation of the GCES phenomenon was validated across species (mouse, sheep,
571 human); (ii) The impact of augmenting GCES via post-hCG glucose administration
572 on luteal function, pregnancy rate, and embryo transfer success was systematically
573 evaluated in mouse/ovine models; (iii) Volunteers undergoing ART treatment were
574 recruited. Following hCG administration, participants received an oral glucose
575 administration at 12 hours to augment GCES. The efficacy of this intervention in
576 enhancing early human luteal function was assessed.

577 **Animals**

578 KM strain mice were sourced from the Center for Animal Testing at Huazhong
579 Agricultural University (Wuhan, China), while *Gys1*$^{floxp/floxp}$ C57BL/6J mice [41] were
580 obtained from GemPharmatech (Nanjing, China). GC-specific deletion of *Gys1* exons
581 6-8 was achieved by crossing *Gys1*$^{floxp/floxp}$ mice with Cyp19a1-Cre transgenic mice [42]
582 (Cyagen; Suzhou, China). All mice were maintained under specific pathogen-free (SPF)
583 conditions with controlled temperature (25 ± 1°C), a 12-hour light/dark cycle, and ad
584 libitum access to food and water. Sheep subjects were housed at Xinjiang Jinken Aoqun
585 Agriculture and Animal Husbandry Technology (Hetian, China) following standard
586 husbandry protocols. Experimental procedures strictly adhered to the institutional
587 guidelines for laboratory animal welfare and were approved by the Animal Ethics
588 Committee of Huazhong Agricultural University (Approval No.: HZAUMO-2023-
589 0115; HZAUSH-2024-0001).

590 **Human clinical trials**

591 Female participants (25-40 years) undergoing ART treatment were prospectively

592 enrolled in this clinical study. Following comprehensive verbal and written disclosure
593 of study objectives, procedures, and potential risks/benefits, written informed consent
594 was obtained from all subjects. At 12 hours post-hCG trigger (Ovidrel®, 250 μg; Sigma,
595 USA), participants were instructed to ingest 75g glucose (Chinaotsuka, China).
596 Transvaginal ultrasound (Voluson™ P8; GE Healthcare, USA)-guided follicular
597 aspiration was performed at 36 hours post-hCG administration to collect luteinizing
598 GCs and follicular fluid from mature pre-ovulatory follicles (16-22 mm diameter). GCs
599 were immediately processed for glycogen quantification and luteal gene expression
600 profiling, while follicular fluid was centrifuged (3,000 ×g, 10 minutes) for subsequent
601 progesterone quantification. The study protocol, designed in accordance with
602 Declaration of Helsinki principles, received prior approval from the Institutional
603 Review Board of Renmin Hospital, Wuhan University (Approval No.: WDRY2024-
604 K262), with continuous monitoring ensuring strict adherence to ethical safeguards
605 regarding patient autonomy and biological sample handling.

606 **Superovulation**

607 Mouse superovulation was induced via intraperitoneal administration of 5 IU pregnant
608 mare serum gonadotropin (PMSG; NSHF, China), followed by 5 IU hCG (NSHF, China)
609 48 hours post-PMSG administration to trigger follicle maturation and subsequent
610 ovulation/luteinization. In sheep, estrus synchronization was achieved through
611 intravaginal insertion of progesterone-impregnated controlled internal drug release
612 (CIDR) devices (Zoetis, USA). Following 10 days of CIDR priming, ewes received 400
613 IU PMSG via intramuscular injection. CIDR removal at 12 days post-insertion
614 coincided with 12.5 μg LH-A3 (NSHF, China) administration to induce
615 ovulation/luteinization. Three timely subcutaneous glucose injections (1.5 g/kg body
616 weight) were administered at 3, 12 and 18 hours post-LH-A3 treatment. Post-mating
617 evaluation included luteal functional assessment through serum progesterone
618 quantification 6 days post-mating and ultimate pregnancy confirmation via
619 ultrasonography (Kxele, China) 30 days post-conception.

620 **Transcriptome analysis**

621 While single-cell RNA-seq enables high-resolution transcriptomic characterization of
622 GCs, its temporal accuracy diminishes in discriminating pre-ovulatory follicle GCs
623 across discrete post-hCG intervals. Conversely, spatial transcriptomics preserves
624 locational fidelity but lacks the resolution of single-cell RNA-seq. To synergize these
625 complementary modalities, we established a spatiotemporal transcriptomic atlas of
626 mouse GCs through multi-omics integration. Mouse ovaries were collected at H0, H1
627 and H6 for single-cell RNA-seq (Yingzi Gene, China). Following cell viability
628 assessment (>85%) and density calibration (1,000 cells/μL), single-cell suspensions
629 were processed on the 10 × Chromium Single Cell Platform (10 × Genomics), involving
630 gel beads in emulsion (GEM) generation, reverse transcription, cDNA amplification,
631 and Illumina-compatible library preparation. Libraries were quantified via Qubit
632 Fluorometry (Thermo, USA) and sequenced on the Illumina Nova6000 platform
633 (Illumina, USA) using 150-base-pair paired-end reads. Raw sequencing data underwent
634 primary analysis using Cell Ranger (v2.1.), performing demultiplexing, genome
635 alignment (GRCm38), Unique Molecular Identifier (UMI), and quality filtering. To
636 reduce dimensionality, the top ten principal components were utilized, and t-Distributed
637 Stochastic Neighbor Embedding (tSNE) was employed. Cell clustering was achieved
638 through a graph-based clustering algorithm, involving the construction of a sparse
639 nearest-neighbor graph followed by Louvain Modularity Optimization [43].
640 Differential gene expression analysis between cell clusters was conducted using the
641 Seurat Bimod test, with significance thresholds set at a false discovery rate (FDR) ≤
642 0.05 and an absolute log2 fold change ≥ 1.5. Spatial transcriptomic data from mouse
643 ovaries were retrieved from the Gene Expression Omnibus (GEO) database
644 (GSE240271), with processed metadata and cell annotation files obtained from the
645 associated GitHub repository (https://github.com/madhavmantri/mouse_ovulation).

646 The integrative analysis commenced with single-cell RNA-seq data preprocessing,
647 where sequencing depth variability was mitigated through total UMI count
648 normalization using *scanpy.pp.normalize_total*. Spatial cell-type mapping was
649 achieved via a PyTorch-implemented deep neural network

650 (*tangram.map_cells_to_space*), trained over 2,000 epochs (learning rate=0.01, Adam
651 optimizer) on 220 ovary-specific marker genes under RNA count-based spatial
652 constraints (*Density_prior='rna_count_based'*). Model optimization targeted
653 minimization of Kullback-Leibler divergence between single-cell RNA-seq and spatial
654 transcriptomic datasets. Cellular annotations (*Subclass_label*) were projected onto
655 spatial coordinates through probabilistic embedding (*tg.project_cell_annotations*), with
656 dominant spot-level cell types resolved via maximum likelihood estimation
657 (*tangram_ct_pred*). Integrated transcriptomes were generated using *tg.project_genes*,
658 followed by multi-level quality control: (i) Training convergence: Visualized via loss
659 function trajectories (*tg.plot_training_scores*); (ii) Cross-platform consistency:
660 Quantified through pairwise gene expression correlation (*tg.plot_genes_sc*); (iii)
661 Spatial fidelity: Validated via AUC metrics for marker gene colocalization
662 (*tg.compare_spatial_geneexp*). Finally, the temporal expression dynamics of genes in
663 GCs post-hCG were profiled using STEM (Short Time-series Expression Miner) with
664 hierarchical clustering (Euclidean distance, complete linkage).
665 Human transcriptome data was extracted from the GEO database, with login
666 numbers GSE133868. GO enrichment analysis of genes was performed through
667 DIAVD database (https://david.ncifcrf.gov/tools.jsp). KEGG enrichment analysis of
668 genes were performed through KOBAS database (http://kobas.cbi.pku.edu.cn/home.d).

669 **Follicle culture**

670 Small antral follicles (250-300 μm diameter) were micro dissected from mouse ovaries
671 using 33-gauge precision needles (KONSFI, China) and subsequently cultured
672 individually in 96-well round bottom cell culture plates (Bkmbio, 110303005, China)
673 under standard conditions (37°C, 5% CO_2, humidified atmosphere). Follicle culture
674 medium consisted of α-MEM (Gibco, C12571500BT, USA) supplemented with 5%
675 FBS (Serana, FBS-AS500, Germany), 1% ITS-G (Thermo, 41400045, USA), 10
676 mIU/mL rFSH (GONAL-f®; sigma, USA), and 100 U/mL penicillin-streptomycin
677 (Servicebio, G4003, China). Following 96 hours of culture, follicles reaching the pre-
678 ovulatory stage were transitioned to high-glucose luteinization induction medium. This

679 medium consisted of α-MEM supplemented with 5mg/mL D-Glucose (MCE, HY-
680 B0389, USA), 1.5 IU/mL rhCG (Ovidrel®; Sigma, USA), 1ng/mL Prolactin (MCE,
681 HY-P700292, USA), 10 μM Cholesterol (MCE, HY-N0322, USA), 1% ITS-G, 5% FBS,
682 10 mIU/mL rFSH, 10 ng/mL hEGF (Thermo, AF-100-15, USA), and 100 U/mL
683 penicillin/streptomycin.

684 **RNA interference**

685 Lentivirus-mediated RNA interference was implemented to achieve targeted gene
686 silencing in follicles or whole ovaries. Gene-specific small interfering RNAs (siRNAs)
687 targeting *Ugp2* (5′-GCAAACTGAGACTGGTGGAAA-3′), *Gys1* (5′-
688 GCCCATGTCTTCACTACCGTA-3′), and *RUNX1* (5′-CGGCAGAACTGAGAAATGCTA-3′)
689 were designed and synthesized by Genepharma (Suzhou, China), with a commercial
690 non-targeting siRNA (MISSION®; Sigma, USA) serving as the negative control. Next,
691 siRNA sequences were cloned into the PLKO.1-EGFP-PURO plasmid (Genecreate,
692 China) under the human U6 promoter. For lentiviral packaging, HEK293T cells (ATCC,
693 USA) were co-transfected in 6-well plates with three plasmids: 0.89 μg siRNA-
694 expressing PLKO.1-EGFP-PURO, 0.44 μg pMD2.G (VSV-G envelope; Addgene,
695 USA), and 0.67 μg pSPAX2 (packaging plasmid; Addgene, USA) using 4 μL
696 jetPRIME® transfection reagent (PolyPlus, 101000046, France). Viral supernatants
697 were harvested 48 hours post-transfection, filtered through 0.45 μm Polyvinylidene
698 Fluoride (PVDF membranes; Sigma, IPVH00010, USA), and clarified by
699 ultracentrifugation (100,000 ×g, 2 hours; Beckman, USA).

700 For in vitro gene knockdown, the isolated small antral follicles were transfected
701 with lentiviral particles (titer: 6.25×10^8 particles/mL) in follicle culture medium
702 supplemented with 10 μg/mL Polybrene (Sigma, TR-1003-G, USA) for 48 hours (37°C,
703 5% CO_2). Transfection was confirmed by EGFP fluorescence visualization. Transfected
704 follicles were subsequently cultured for 48 hours to reach the pre-ovulatory stage,
705 followed by transfer to high-glucose luteinization medium for terminal stimulation.
706 Samples were collected at predefined intervals for analysis.

707 For in vivo ovarian-specific knockdown, fifteen-day-old mice were anesthetized

708 with 1% pentobarbital sodium (50 mg/kg; Sigma, USA). A total of 5 μL high-titer
709 lentivirus (titer: 6.25×10^9 particles/mL) was bilaterally microinjected beneath the
710 ovarian bursa using a Hamilton 701N syringe (10 μL capacity; 80330, Switzerland)
711 coupled to a 33-gauge RN needle (Hamilton, 7803-05, Switzerland). Control cohorts
712 received equivalent volumes of non-targeting siRNA lentivirus. Mice were allowed to
713 recover for 5 days prior to experimental analyses to ensure stable gene knockdown.

714 **Metabolic flux assay**

715 Pre-ovulatory follicles (550-600 μm diameter) were micro dissected from mouse
716 ovaries and preconditioned in glucose-depleted Dulbecco's Modified Eagle Medium
717 (DMEM; Gibco, 11966-025, USA) for 2 hours to deplete endogenous glucose.
718 Following depletion, follicles were cultured for 6 hours in luteinization medium
719 containing 2 mg/mL uniformly labeled $^{13}C_6$-glucose (^{13}C-glucose; MCE, HY-B0389A,
720 USA) to achieve isotopic labeling of glycolytic intermediates. Metabolic flux analysis
721 was performed by Biotree (Shanghai, China). GCs isolated from the follicles underwent
722 cryogenic homogenization in liquid nitrogen, followed by suspension in 1 mL of pre-
723 chilled (−40°C) 50% methanol. After two sequential freeze-thaw cycles (dry ice/ice
724 bath), phase separation was achieved by adding 0.4 mL chloroform with vigorous
725 vortexing (30 sec) and centrifugation (12,000 ×g, 15 minutes, 4°C). The polar
726 metabolite-enriched aqueous phase was analyzed via hydrophilic interaction liquid
727 chromatography (HILIC) on an XBridge BEH Amide column (150 × 2.1 mm, 2.5 μm;
728 Waters, USA) coupled to a Q Exactive™ Plus Orbitrap mass spectrometer (Thermo,
729 USA) operated in negative electrospray ionization (ESI^-) mode. Chromatographic
730 gradient employed: solvent A (20 mM NH_4Ac/NH_4OH in water:acetonitrile, 95:5) and
731 solvent B (acetonitrile). Gradient program: 0-3 minutes (10% A, 90% B), 3-8 minutes
732 (25% A, 75% B), 8-10 minutes (30% A, 70% B), 10-13 minutes (50% A, 50% B), 13-
733 16 minutes (75% A, 25% B), 16-20.5 minutes (100% A, 0% B), 20.5-25 minutes (10%
734 A, 90% B) at a flow rate of 0.15 mL/minutes and column temperature of 25°C. Mass
735 spectrometric parameters included: Resolution, 140,000 (at m/z 200); Automatic gain
736 control (AGC) target, 1×10^6 ions; scan range, m/z 75–1000; Column temperature:

737 25°C. ^{13}C-isotopologue distributions were deconvoluted using El-MAVEN v.12.0,
738 incorporating MATLAB (v2021b)-based algorithms for natural isotopic abundance
739 correction to enable quantitative determination of metabolic flux through central carbon
740 pathways.

741 **Quantification of ^{13}C-Glucose incorporated into glycogen**

742 The isolated pre-ovulatory follicles were preconditioned in glucose-depleted DMEM
743 for 2 hours. Subsequently, follicles were incubated for 6 hours in luteinization medium
744 supplemented with 2 mg/mL ^{13}C-glucose to facilitate isotopic incorporation into
745 glycogen. Post-culture, GCs were isolated from follicles, homogenized in ultrapure
746 water, and partitioned into paired aliquots. The experimental aliquot was subjected to
747 acid hydrolysis using 6 M trifluoroacetic acid (TFA; 100°C, 4 hours) to depolymerize
748 glycogen and release bound glucose monomers, while the paired control aliquot
749 remained unhydrolyzed to quantify background glucose levels. Following hydrolysis,
750 samples were equilibrated to ambient temperature (25 ± 1°C) and lyophilized under
751 reduced pressure (300 mbar, 52°C) using a rotary evaporator (Heidolph, Germany).
752 Dried residues were reconstituted in 0.5 M methanolic 1-phenyl-3-methyl-5-
753 pyrazolone (PMP) solution, followed by the addition of an equimolar volume of
754 aqueous ammonia (28%, pH 12.5) to initiate derivatization. The mixture was vortexed
755 and incubated at 70°C for 90 minutes to form glucose-PMP derivatives. Post-
756 derivatization, samples underwent three sequential purification cycles, each involving
757 resuspension in 1 mL ultrapure water followed by rotary evaporation (300 mbar, 40°C)
758 to remove residual ammonia. ^{13}C-glucose-PMP adducts were then extracted via
759 biphasic partitioning (chloroform/water; 1:1 v/v), with the aqueous phase collected for
760 ultra-performance liquid chromatography coupled to quadrupole time-of-flight mass
761 spectrometry (UPLC-QTOF-MS; Waters, USA) analysis. Chromatographic separation
762 was performed on an ACQUITY C18 column (100 × 2.1 mm, 1.7 μm; Waters, USA)
763 maintained at 45°C using a binary gradient consisting of solvent A (0.1% formic acid
764 in water) and solvent B (acetonitrile) at a flow rate of 0.4 mL/minutes. Gradient
765 program: 0-1 minutes (99% A, 1% B); 1-2 minutes (80% A, 20% B); 2-5 minutes (60%

766 A, 40% B); 5-6 minutes (45% A, 55% B); 6-13 minutes (20% A, 80% B); 13-17 minutes
767 (5% A, 95% B); 17-20 minutes (99% A, 1% B). Sample injection volume was 1 μL.
768 Mass spectrometric detection was performed in positive electrospray ionization (ESI^+)
769 mode with a scan range of m/z 50-1200. Instrument parameters included: desolvation
770 gas flow, 500 L/hour at 400°C; cone gas flow, 50 L/hour; source temperature, 100°C;
771 capillary voltage, 1000 V; cone voltage, 30 V; acquisition rate, 0.3 sec with no inter-
772 scan delay. The sample cone voltage was optimized using the instrument's tune page.
773 Accurate mass measurement and elemental composition determination for precursor
774 and fragment ions were conducted using MassLynx 4.1 software (Waters, USA), with
775 ^{13}C-glucose of glycogen calculated as: experimental aliquot ^{13}C-glucose - control
776 aliquot ^{13}C-glucose.

777 **Metabolite analysis**

778 Metabolomic profiling was performed by Majorbio (Shanghai, China). GCs isolated
779 from pre-ovulatory follicles at specified post-hCG timepoints (H0 and H6) were mixed
780 with ice-cold methanol: water (4:1, v/v) extraction solvent (containing 0.02 mg/mL 2-
781 chloro-L-phenylalanine as internal standard). Homogenization used a Wonbio-96c
782 tissue grinder (wonbio, China) at 50 Hz for 6 minutes (-10°C), followed by 30-minutes
783 ultrasonic extraction (5°C, 40 kHz) and centrifugation (13,000 ×g, 15 minutes, 4°C) to
784 collect supernatants for injection. Analysis employed a Thermo Scientific™ Vanquish
785 UHPLC coupled to Q Exactive™ HF-X system (Thermo, USA) with heated
786 electrospray ionization (HESI) source operated in polarity switching mode.
787 Chromatographic separation used an ACQUITY UPLC HSS T3 column (100 mm × 2.1
788 mm, 1.8 μm; Waters, USA) with mobile phase A (0.1% formic acid in water: acetonitrile,
789 2:98) and B (0.1% formic acid in acetonitrile) at 0.4 mL/minutes, column temperature
790 40°C, and injection volume 5 μL. The gradient program was: 0-2 minutes (95%A, 5%B);
791 2-14 minutes (5%A, 95%B); 14-14.1 minutes (95%A, 5%B); 14.1-17 minutes (95%A,
792 5%B). Mass spectrometry parameters: full MS resolution 120,000 (@ m/z 200), dd-
793 MS^2 resolution 30,000 (@ m/z 200), scan range m/z 70-1050, spray voltage +3.5 kV/-
794 2.8 kV, capillary temperature 400°C, sheath gas 40 arb, aux gas 10 arb, S-lens RF 55%.

795 Quality control employed pooled QC samples injected every 10 experimental samples
796 with retention time deviation < 0.1 minutes and peak intensity RSD < 15%. Raw data
797 processing used Progenesis QI v3.0 (Waters, USA) for peak extraction (S/N threshold >
798 3), alignment (5 ppm mass tolerance), and normalization (internal standard correction).
799 Statistical analysis on Majorbio Cloud Platform (https://cloud.majorbio.com), in GPI-
800 anchor biosynthesis pathway annotated using KEGG database (https://www.kegg.jp/).

801 **Analysis of glucose uptake capacity**

802 The glucose uptake capacity of GCs was quantified using the fluorescent D-glucose
803 analog 2-NBDG (MCE, HY-116215, USA). Briefly, GCs were isolated from pre-
804 ovulatory follicles at specified post-hCG timepoints, washed twice with phosphate-
805 buffered saline (PBS; pH 7.4), and resuspended in pre-warmed (37°C) 2-NBDG
806 working solution (100 μM in glucose-depleted DMEM). Following 30-minutes
807 incubation at 37°C under 5% CO_2, GCs were pelleted by centrifugation (600 ×g, 5
808 minutes), washed twice with ice-cold PBS to terminate uptake, and finally resuspended
809 in PBS. Fluorescence intensity of internalized 2-NBDG, which directly correlates with
810 cellular glucose uptake capacity, was measured using a BD FACSAria™ III flow
811 cytometer (BD Biosciences, USA) equipped with a 488-nm laser and 530/30-nm
812 emission filter. 20,000 viable cells *per* sample were acquired. Data analysis was
813 performed using FlowJo v10.4.0 software (BD Biosciences, USA), with results
814 expressed as geometric mean fluorescence intensity (MFI).

815 **Transmission electron microscope**

816 Pre-ovulatory follicles isolated from mouse ovaries at designated post-hCG timepoints
817 were processed for transmission electron microscopy analysis. Follicles were primarily
818 fixed by immersion in 2.5% (v/v) glutaraldehyde (SPI Chem, USA) at 4°C for 12 hours.
819 Subsequently, samples were rinsed thrice with 0.1 M PBS (pH 7.4) and post-fixed with
820 1% (w/v) osmium tetroxide (OsO_4; SPI Chem, USA) in PBS for 2 hours at 4°C.
821 Thereafter, specimens were dehydrated through a graded ethanol series (30%, 50%,
822 70%, 90%, 100%; Sinopharm, China), transitioned to propylene oxide, and infiltrated
823 with Spurr's epoxy resin (SPI Chem, USA) using ascending resin:propylene oxide ratios

824 (1:3, 1:1, 3:1 v/v). Pure resin-embedded samples were polymerized at 60°C for 48 hours.
825 Ultrathin sections (60 nm thickness) were cut using a diamond knife on a Leica UC7
826 ultramicrotome (Leica, Germany), mounted on 200-mesh copper grids, and double-
827 stained with 2% (w/v) uranyl acetate (SPI Chem, USA) for 30 minutes followed by
828 Reynolds' lead citrate for 5 minutes. Ultrastructural examination of GCs was performed
829 using a HT7800 transmission electron microscope (Hitachi, Japan) operated at 80 kV.
830 Digital images were acquired using an CCD camera (Gatan, USA) with standardized
831 exposure settings.

832 **PAS Staining**

833 Glycogen deposition in tissues was assessed using Periodic Acid-Schiff Staining Kit
834 (Sigma, 395B-1KT, USA). According to manufacturer's specifications, ovarian samples
835 were fixed in a 4% paraformaldehyde solution (Servicebio, G1101, China) containing
836 30% sucrose for 48 hours at 4°C. Post-fixation, samples were embedded in Optimal
837 Cutting Temperature (OCT) compound (Sakura, 4583, USA). The cultured follicles
838 were directly embedded in OCT. 6-μm-thick cryosections were prepared using a
839 freezing microtome (Leica, Germany) maintained at -20°C. Sections were washed in
840 PBS (3 × 5 minutes), post-fixed with 4% paraformaldehyde for 20 minutes at room
841 temperature, and rinsed in PBS (3 × 5 minutes). Subsequently, sections were oxidized
842 in periodic acid solution for 10 minutes, rinsed in PBS (5 minutes), stained with Schiff's
843 reagent for 25-30 minutes in the dark, and washed in PBS for 5 minutes. Imaging was
844 performed using a microscope (Olympus, Japan) equipped with a digital camera under
845 200 × magnification.

846 **Immunofluorescence staining**

847 Ovaries collected at designated post-hCG timepoints were fixed in 4%
848 paraformaldehyde for 48 hours at 4°C, dehydrated through graded ethanol series,
849 cleared in xylene, and embedded in paraffin. 3-μm-thick sections were prepared using
850 a rotary microtome (Leica, Germany). Sections were deparaffinized in xylene (2 × 10
851 minutes), rehydrated through descending ethanol gradients, and subjected to heat-
852 induced epitope retrieval in sodium citrate buffer (Solarbio, C1032, China) at 98°C for

853 30 minutes. After cooling to room temperature, sections were blocked with 10% (v/v)
854 normal goat serum (Boster, AR0009, China) in PBS for 60 minutes at room temperature.
855 Subsequently, sections were incubated with rabbit anti-CD34 monoclonal primary
856 antibody (1:300 dilution; Abclonal, A19015, China) diluted in SuperKine™ Enhanced
857 Antibody Dilution Buffer (Abbkine, BMU103, China) for 12 hours at 4°C in a
858 humidified chamber. Following three washes in PBS (5 minutes each), sections were
859 incubated with Alexa Fluor® 594-conjugated goat anti-rabbit IgG secondary antibody
860 (1:200 dilution; Abclonal, AS039, China) for 60 minutes at room temperature protected
861 from light. Nuclei were counterstained with 10 μg/mL 4′,6-diamidino-2-phenylindole
862 (DAPI; Biosharp, BL105A, China) for 10 minutes. After final PBS washes (3 × 5
863 minutes), sections were mounted with antifade mountant (Servicebio, G1401, China)
864 and imaged using a confocal laser scanning microscope (Zeiss, Germany) equipped
865 with 405-nm (DAPI) and 561-nm (Alexa Fluor® 594) lasers. Images were acquired at
866 200 × magnification and processed using ZEN 2.3 lite software (Zeiss, Germany).

867 **Lysosome analysis**

868 Lyso-Tracker Green (Beyotime, C1047S, China) was utilized for lysosome
869 quantification analysis. Following the manufacturer's protocol, GCs were isolated from
870 pre-ovulatory follicles at specified post-hCG timepoints, washed with HBSS (Beyotime,
871 C0218, China). Subsequently, GCs were stained with the Lyso-Tracker Green working
872 solution and incubated at 37°C for 30 minutes. Fluorescence values were measured
873 using a flow cytometry instrument (BD Biosciences, USA), and data analysis was
874 conducted through FlowJo 10.4. GCs with Lyso-tracker (FITC) fluorescence > 3×10^3,
875 defined using a threshold slightly above the negative control maximum, were termed
876 high Lyso-tracker fluorescence GCs.

877 **Analysis of lysosomal acid phosphatase activity**

878 Lysosomal acid phosphatase activity in GCs isolated from pre-ovulatory follicles at
879 designated post-hCG timepoints was determined using an Acid Phosphatase Activity
880 Assay Kit (Boxbio, AKFA017C, China). According to manufacturer’s instructions,
881 GCs were resuspended in 100 μL of lysis buffer and mechanically homogenized.

882 Lysates were centrifuged at 8,000 ×g for 10 minutes at 4°C to obtain supernatants.
883 Aliquots (20 μL) of the supernatant were incubated with ACP working solution for 15
884 minutes at 37°C. Following enzymatic reactions, ACP chromogenic substrate was
885 added and the mixture was incubated at room temperature for 10 minutes to develop
886 color. Absorbance at 510 nm were measured using a Spark Multimode Microplate
887 Reader (Tecan, Switzerland). Enzymatic activities were calculated from a 6-point
888 standard curves (0.5-8.0 μmol/mL) and expressed as U per g protein, with protein
889 concentrations determined via bicinchoninic acid (BCA) assay kit (Servicebio, G2026,
890 China).

891 **MMP assay**

892 MMP was quantified using a JC-1-based Mitochondrial Membrane Potential Assay Kit
893 (Solarbio, M8650, China). According to manufacturer's instructions, isolated GCs were
894 resuspended in pre-warmed (37°C) assay buffer and incubated with 10 μM JC-1
895 working solution for 20 minutes at 37°C under 5% CO_2 in the dark. Subsequently, cells
896 were pelleted by centrifugation (600 ×g, 10 minutes), washed twice with ice-cold JC-1
897 staining buffer, and resuspended in fresh assay buffer. Fluorescence intensities were
898 measured using the Spark Multimode Microplate Reader with the following settings:
899 excitation/emission = 485/535 nm (green monomeric form) and 535/590 nm (red J-
900 aggregates). MMP was expressed as the ratio of red (590 nm) to green (535 nm)
901 fluorescence intensity, where decreased ratios indicate mitochondrial depolarization.

902 **ATP quantification**

903 ATP levels in GCs were quantified using an ATP Determination Kit (Thermo, A22066,
904 USA) based on firefly luciferase chemiluminescence. According to manufacturer's
905 instructions, isolated GCs were lysed in 60 μL ice-cold ATP extraction buffer by
906 homogenizing followed by 5-minutes incubation on ice. Lysates were centrifuged
907 (10,000 ×g, 4°C, 5 minutes) to remove insoluble debris. Background ATP in 96-well
908 opaque plates (Corning, 3915, USA) was quenched by incubating with 100 μL ATP
909 detection working solution for 5 minutes at room temperature. Subsequently, 20 μL
910 supernatant of cell lysates was mixed with 100 μL ATP detection working solution.

911 Chemiluminescence signals (relative light units, RLU) were immediately measured
912 using the Spark Multimode Microplate Reader. ATP concentrations were interpolated
913 from a 6-point standard curve (0-0.64 nmol/mL) and normalized to total protein content,
914 with results expressed as pmol/mg protein.

915 **Quantification of NAD^+/NADH ratio**

916 The NAD^+/NADH ratio in GCs was determined using a NAD^+/NADH Assay Kit
917 (Beyotime, S0175, China) based on alcohol dehydrogenase (ADH)-coupled WST-8
918 reduction. According to manufacturer's instructions, GCs were lysed in 120 μL ice-cold
919 extraction buffer and centrifuged (10,000 ×g, 4°C, 10 minutes). For total NAD
920 (NAD^++NADH) quantification, 20 μL supernatant was mixed with 90 μL NADH
921 working solution and 10 μL WST-8 chromogen, then incubated at 37°C for 30 minutes.
922 For NADH-specific quantification, an identical aliquot was heated at 60°C for 30
923 minutes to decompose NAD^+ prior to reagent addition. Post-decompose, 20 μL
924 supernatant was mixed with 90 μL ADH working solution and 10 μL WST-8 chromogen,
925 then incubated at 37°C for 30 minutes. Absorbance at 450 nm was measured using the
926 Spark Multimode Microplate Reader. NAD^+ and NADH concentrations were
927 interpolated from an 8-point NADH standard curve (0-8 nmol/mL), with NAD^+
928 calculated as: Total NAD - NADH. Results were normalized to total protein
929 concentration.

930 **Quantification of glycogen, free fatty acids and triglycerides**

931 GCs isolated from pre-ovulatory follicles at designated post-hCG timepoints were
932 analyzed for glycogen, free fatty acids, and triglycerides using standardized
933 biochemical assays. Glycogen content was determined with a Glycogen Assay Kit
934 (Solarbio, BC0340, China) based on enthrone colorimetric method. According to
935 manufacturer's instructions, GCs were homogenized in extraction buffer, sonicated (35%
936 amplitude, 10 sec pulse × 3; Sonics & Materials Inc, USA), and boiled for 20 minutes.
937 After centrifugation (10,000 ×g, 4°C, 10 minutes), 60 μL supernatant was mixed with
938 240 μL detection buffer and incubated in boiling water for 10 minutes. The absorbance
939 at 620 nm was measured using the Spark Multimode Microplate Reade. Free fatty acids

940 were measured using a Free Fatty Acid Quantification Kit (Boxbio, AKFA008C, China)
941 based on copper soap colorimetry. GCs were homogenized in lysis buffer and
942 centrifuged (10,000 ×g, 4°C, 10 minutes). The supernatant was mixed with extraction
943 buffer by vortexing for 10 minutes. After centrifugation (3,000 ×g, 25°C, 10 minutes),
944 the supernatant was mixed with detection buffer and incubated in room temperature for
945 10 minutes. Absorbance at 550 nm was measured against palmitic acid standards (0.05-
946 1.00 μmol/mL). Triglyceride content was assessed via Triglyceride Assay Kit (Njjcbio,
947 A110-1-1, China) employing GPO-PAP methodology: GCs were lysed in RIPA buffer
948 containing 1 × protease/phosphatase inhibitor (Proteintech, PR20038, China), sonicated
949 (35% amplitude, 10 sec pulse × 3), and centrifuged (10,000 ×g, 4°C, 15 minutes). 10
950 μL supernatant was mixed with 200 μL enzymatic working solution and incubated at
951 37°C for 10 minutes. Absorbance was measured at 500 nm. All values were normalized
952 to total protein, with results expressed as mg/g protein (Glycogen), μmol/g protein (Free
953 Fatty Acids and triglyceride).

954 **Progesterone determination**

955 Serum, follicular fluid and culture medium samples were clarified by centrifugation
956 (3,000 ×g, 4°C, 10 minutes), while ovarian tissues were homogenized in ice-cold PBS
957 and centrifuged (10,000 ×g, 4°C, 10 minutes). Resulting supernatants were aliquoted
958 and stored at -80°C until analysis. Progesterone concentrations were quantified via
959 radioimmunoassay (RIA) performed by Beijing North Institute of Biological
960 Technology, a certified clinical testing laboratory (Beijing, China) using a commercial
961 RIA kit with validated sensitivity (2 pg/mL). The assay employed competitive binding
962 between endogenous progesterone and ^{125}I-labeled progesterone tracer for anti-
963 progesterone polyclonal antibody binding sites. Following 1 hour incubation at 37°C,
964 antibody-bound fractions were separated using polyethylene glycol precipitation.
965 Radioactivity was measured for 1 minute per tube in a γ-counter (PerkinElmer, USA).
966 Standard curves (0-100 ng/mL) were established with each run, and ovarian
967 progesterone levels were normalized to tissue weight (ng progesterone/g ovarian tissue).

968 **Pharmaceutical intervention protocols**

969 All compounds were procured from MCE. Stock solutions were prepared according to
970 manufacturers' specifications and diluted in appropriate vehicles immediately prior to
971 use. In vivo inhibition of glycogenolysis: Ingliforib (HY-19396) dissolved in 10%
972 DMSO/90% corn oil was administered via intraperitoneal injection (100 μL, 15 mg/kg)
973 9 hours post-hCG injection. In vitro modulation: 40 nM insulin (HY-P0035) was
974 supplemented into the luteinization medium to activate insulin signaling, while 100 nM
975 BMS-536924 (HY-10262) was used to suppress this signaling. MAPK pathway was
976 activated by 10 μM C16-PAF (HY-108635), whereas suppressed by 40 μM U0126 (HY-
977 12031A). All compounds were filter-sterilized (0.22 μm; Sigma, SLGV004SL, USA)
978 and controls included equivalent vehicles.

979 **Western blotting**

980 Total proteins were extracted using RIPA lysis buffer (Thermo, 89901, USA)
981 supplemented with 1 × protease/phosphatase inhibitor and 1 mM PMSF (Thermo,
982 36978, USA) on ice. Lysates were centrifuged (10,000 ×g, 4°C, 15 minutes) and
983 supernatants quantified via BCA assay kit. Equal protein loads (20 μg/lane) were
984 resolved on SDS-polyacrylamide gels at 80 V (stacking) and 120 V (resolving) in Tris-
985 Glycine-SDS buffer (25 mM Tris, 250 mM glycine, 0.1% SDS, pH 8.3) and transferred
986 to 0.45 μm PVDF membranes at 72 V for 100 minutes in transfer buffer (48 mM Tris,
987 39 mM glycine, 0.037% SDS, 10% methanol). Membranes were blocked with 5% non-
988 fat dry milk (Nestlé, Switzerland) in TBST (Servicebio, G0004, China) for 1 hour at
989 room temperature, then incubated overnight at 4°C with primary antibodies diluted in
990 SuperKine™ Enhanced Antibody Dilution Buffer: phospho-PKCα (CST, #9375,
991 1:1000), SLC2A1 (Proteintech, 21829-1-AP, 1:1000), GYS1 (CST, #3886, 1:1000),
992 GSK3B (CST, #12456, 1:1000), phospho-GYS1 (CST, #47043, 1:1000), phospho-
993 GSK3β (CST, #9323, 1:1000), PYGB (Proteintech, 12075-1-AP, 1:1000), UGP2
994 (Proteintech, 10391-1-AP, 1:800), INSR/IGF1R (Abclonal, A21984, 1:1000), phospho-
995 INSR/IGF1R (CST, #3024, 1:800), RUNX1 (Proteintech, 25315-1-AP, 1:1000),
996 ERK1/2 (Abclonal, A4782, 1:1000), phospho-ERK1/2 (CST, #9101, 1:1000), GAPDH

997 (Abclonal, AC002, 1:5000). After TBST washes (3 × 10 minutes), membranes were
998 incubated with species-matched HRP-conjugated secondary antibodies (goat anti-
999 rabbit IgG, BF03008; goat anti-mouse IgG, BF03001; Biodragon, 1:4000) for 1 hour at
1000 25°C. Following TBST washes (3 × 10 minutes), signals were developed with
1001 SuperSignal™ West Pico PLUS Chemiluminescence Kit (Thermo, 34580, USA) and
1002 captured using a Tanon-5200 Chemiluminescence Imager (Biotanon, China).
1003 Uncropped blots are presented in Supplementary Figure S10.

1004 **Lectin binding assay**

1005 For lectin blotting, GCs collected at H0, H1 and H6 were homogenized in ice-cold
1006 PIERCE™ IP Lysis Buffer (Thermo, 87787, USA) supplemented with 1 ×
1007 protease/phosphatase inhibitor and 1 mM PMSF. Lysates were incubated at 4°C for 30
1008 minutes with end-over-end rotation, then centrifuged at 10,000 ×g for 15 minutes at
1009 4°C. Supernatants were quantified using BCA assay kit. Equal protein was resolved on
1010 SDS-polyacrylamide gels at 80 V (stacking) and 120 V (resolving) in Tris-Glycine-SDS
1011 buffer and transferred to 0.45 μm PVDF membranes at 72 V for 100 minutes in transfer
1012 buffer. Membranes were blocked with 1 × Carbo-Free™ Blocking Solution (Vector,
1013 SP-5040, USA) for 1 hour at 25°C with agitation, then incubated with 1 μg/mL
1014 Biotinylated-Concanavalin A (MCE, HY-NP0174, USA)/Biotinylated-Peanut
1015 Agglutinin (MCE, HY-NP0182, USA) in blocking buffer for 1 hour at 25°C. After
1016 TBST washes, membranes were probed with Streptavidin-HRP (Thermo, N100; 1:4000
1017 dilution in blocking buffer) for 1 hour at 25°C. Following additional TBST washes,
1018 signals were developed using SuperSignal™ West Pico PLUS Chemiluminescent
1019 Substrate and captured using a Tanon-5200 Chemiluminescence Imager with automatic
1020 gain control. Full uncropped blots are provided in Supplementary Figure S10.

1021 For lectin flow cytometry assay, GCs were isolated from H0, H1 and H6 ovaries
1022 and washed twice with ice-cold PBS. Cells were incubated with FITC labeled MALI
1023 (Vector, FL-1311, USA)–20 μg *per* 10^6 cells concentration in 1 × Carbo Free blocking
1024 buffer for 20 minutes at room temperature. Finally, cells were diluted to 10^6/mL using
1025 1 × Carbo Free blocking buffer and analyzed using a Cytek® Aurora Full Spectrum

1026 Flow Cytometry (Cytek, USA) equipped with a 488-nm laser and 520-nm emission
1027 filter. 10,000 viable cells *per* sample were acquired. Data analysis was performed using
1028 FlowJo v10.4.0 software, with results expressed as geometric MFI.

1029 **EMSA protocol**

1030 Mouse RUNX1 coding sequence (NCBI RefSeq: NM_001111021) was cloned into
1031 pcDNA3.1-3XFlag plasmid (Addgene, China) for eukaryotic expression. Flag-tagged
1032 RUNX1 protein was immunoprecipitated from HEK293T cell lysates using anti-Flag
1033 M2 affinity gel (Sigma, A2220, USA) with three wash cycles in TBST. Bound proteins
1034 were eluted with 0.1 M glycine (pH 2.7) and immediately neutralized with a
1035 neutralization buffer (1 M Tris, pH 8.5). JASPAR web-based platform
1036 (https://jaspar.elixir.no/) was employed to predict the direct binding sites of RUNX1
1037 within the promoter regions of the *Insr* and *Igf1r*. Based on the predicted motifs,
1038 double-stranded DNA probes and corresponding site-directed mutant probes were
1039 designed, and subsequently synthesized by Genecreate (Wuhan, China). EMSA was
1040 conducted using a Chemiluminescent EMSA Kit (Beyotime, GS009, China). According
1041 to manufacturer's instructions, biotinylated double-stranded DNA probes containing
1042 consensus RUNX-binding motifs were incubated with purified Flag-RUNX1 (100 ng)
1043 in binding buffer for 30 minutes at room temperature. Protein-DNA complexes were
1044 resolved on 6% non-denaturing polyacrylamide gels (29:1 acrylamide:bis) in TBE
1045 buffer (Beyotime, R0223, China) at 100 V for 60 minutes at 4°C. Electrophoretically
1046 transferred to Hybond-N^+ membranes (Cytiva, RPN1510B, USA) at 380 mA for 45
1047 minutes in TBE buffer, complexes were UV-crosslinked (120 mJ/cm², 60 ses), after
1048 blocking with the streptavidin-HRP working solution, the shift-band was detected using
1049 ECL chemiluminescent reagent by exposure on a Tanon-5200 Chemiluminescence
1050 Imager. The probe sequences are provided in Table S2.

1051 **Luciferase reporter assay**

1052 The promoter regions of *Insr* (chr8: 3,171,461-3,172,061 bp) and *Igf1r* (chr7:
1053 67,600,075-67,602,575 bp) were PCR-amplified from mouse genomic DNA and
1054 inserted into the PGL3-Basic luciferase reporter vector (Promega, USA) using the

1055 ClonExpress Ultra One Step Cloning Kit (Vazyme, C115-01, China). Site-directed
1056 mutagenesis of RUNX1-binding motifs (core sequence: 5′-TGTGGT-3′→5′-TGTAGT-
1057 3′) was performed using Mut Express II Fast Mutagenesis Kit (Vazyme, C214-01,
1058 China) with verification by sanger sequencing. HEK293T cells seeded in 24-well plates
1059 (1×10^5 cells/well) were transfected after 24 hours using jetPRIME® reagent with the
1060 following plasmid ratio per well: 250 ng pGL3-*Insr*/pGL3-*Igf1r* (wild-type or mutant),
1061 250 ng RUNX1-pcDNA3.1 or empty vector, and 2.5 ng pRL-TK Renilla*luciferase
1062 control vector (Promega, USA). After 24-hours incubation, cells were lysed in 100 μL
1063 Passive Lysis Buffer and analyzed using the Dual-Luciferase Reporter Assay System
1064 (Promega, E1910, USA). Firefly luciferase activity was measured first using the Spark
1065 Multimode Microplate Reader, followed by Renilla luciferase quantification after Stop
1066 & Glo® reagent addition. Promoter activity was expressed as Firefly/Renilla
1067 luminescence ratio normalized to empty vector control. Primers are listed in
1068 Supplementary Table S2.

1069 **SEAP reporter assay**

1070 A codon-optimized SEAP gene sequence [44] was cloned into the pCDH-CMV-MCS-
1071 EF1-copGFP-T2A-Puro plasmid (GeneCreate, China), followed by lentiviral
1072 packaging in HEK293T cells and concentration by ultracentrifugation to obtain high-
1073 titer lentivirus. Small antral follicles were transfected with lentivirus (titer: 6.25×10^9
1074 particles/mL) to overexpress SEAP, with successful transfection confirmed by EGFP
1075 fluorescence. Upon reaching the pre-ovulatory stage, follicles were transferred to
1076 luteinization medium for 6 hours. Next, GCs were isolated by mechanical dissection
1077 and cultured in fresh follicle medium for another hour. Following centrifugation (3,000
1078 ×g, 10 minutes, 4°C), the GC pellets were lysed in RIPA buffer for BCA assay, while
1079 the supernatants were aspirated for SEAP assay using Phospha-Light™ SEAP Reporter
1080 Assay kit (Thermo, T1015, USA). According to manufacturer's instructions, the
1081 supernatants were diluted 1:1 in 1 × dilution buffer, heat-inactivated at 65 ± 0.5°C for
1082 30 minutes, cooled to 25°C, then 50 μL sample mixed with 50 μL assay buffer (5
1083 minutes, 25°C), followed by 50 μL reaction substrate (20 minutes, 25°C in dark).

1084 Chemiluminescence (relative light units, RLU) was measured using the Spark
1085 Multimode Microplate Reader. SEAP activity was normalized to total protein content.

1086 **qRT-PCR assay**

1087 Total RNA was isolated using TRIzol™ Reagent (Takara, 9109, Japan) and quantified
1088 with a NanoDrop 2000 spectrophotometer (Thermo, USA). Reverse transcription was
1089 performed with 1 μg total RNA using Evo M-MLV RT Kit with gDNA clean (AGbio,
1090 AG11728, China) in 20 μL reactions (37°C for 15 minutes, 85°C for 5 sec). qPCR was
1091 conducted in triplicate on a CFX384/96 Touch™ Real-Time PCR System (Bio-Rad,
1092 USA) with 10 μL reaction volumes containing: 5 μL SYBR Green Premix Pro Taq HS
1093 (AGbio, AG11739, China), 4 μL cDNA template and 250 nM gene-specific primers (1
1094 μL). Thermal cycling parameters: initial denaturation at 95°C for 15 minutes; 35 cycles
1095 of 95°C for 10 sec and 60°C for 30 sec (combined annealing/extension); followed by
1096 melt curve analysis (60°C to 95°C, increment 0.5°C/5 sec). Specificity was confirmed
1097 by single-peak melt curves of PCR products. Relative mRNA expression was calculated
1098 by the $2^{-\Delta\Delta Ct}$ method using *Actb* or *Gapdh* as endogenous controls. Amplified products
1099 were visualized through agarose gel electrophoresis (80V, 80 mA, 75 minutes). The
1100 primer sequences are provided in Table S2.

1101 **ChIP-qPCR assay**

1102 ChIP-qPCR was performed using GCs isolated from pre-ovulatory follicles at specified
1103 post-hCG intervals (H0, H6). Cells were fixed in 10 mL DMEM/F-12 (Gibco,
1104 11320033, USA) containing freshly prepared 1% formaldehyde (CST, 12606S, USA)
1105 for 10 minutes at room temperature with rotation (15 rpm). Fixation was quenched by
1106 adding 1 mL 1.5 M glycine followed by 5 minutes rotation. Cell pellets were washed
1107 thrice with ice-cold PBS in 1.5 mL centrifuge tubes (Axygen, MCT-150-C, USA), then
1108 lysed in pre-chilled cytomembrane lysis buffer (10 mM HEPES pH 7.9, 0.5% IGEPAL-
1109 CA630, 1.5 mM $MgCl_2$, 10 mM KCl, 1 × protease inhibitor cocktail [Abclonal,
1110 RM02916, China]) for 15 minutes at 4°C with vortex agitation (10 sec/5 minutes
1111 interval). Nuclear lysis was conducted in pre-chilled buffer (0.5% SDS, 10 mM EDTA,
1112 50 mM Tris-HCl pH 8.1, 1 × protease inhibitor cocktail) for 15 minutes at 4°C.

1113 Chromatin was sonicated using a ultrasonic disintegrator (Bioruptor Plus; Belgium)
1114 with 30 sec ON/30 sec OFF cycles (30 cycles total) in 4°C water bath to generate 200-
1115 500 bp fragments validated by agarose electrophoresis. Sonicated lysates were
1116 centrifuged at 10,000 ×g for 2 minutes at 4°C, and supernatants diluted 1:10 in ChIP IP
1117 buffer (0.01% SDS, 1% Triton X-100, 2 mM EDTA, 50 mM Tris-HCl pH 8.0, 150 mM
1118 NaCl, 1 × protease inhibitor cocktail). For immunoprecipitation, pre-cleared chromatin
1119 was incubated with 5 μg anti-RUNX1 antibody (Proteintech, 25315-1-AP, China) or
1120 species-matched IgG control (Abcam, ab172730, UK) conjugated to protein A/G
1121 Dynabeads (Thermo, 26162, USA) with rotation overnight at 4°C. The beads were
1122 washed, eluted, and reverse cross-linked. DNA purification was performed using the
1123 QIAquick® PCR Purification Kit (QIAGEN, 28104, Germany). Subsequently, the
1124 DNA was utilized for qPCR analysis with specific primers. Amplified products were
1125 visualized through agarose gel electrophoresis (80V, 80 mA, 75 minutes). The primer
1126 sequences are detailed in Table S2.

1127 **Embryo transfer**

1128 Donor female mice (KM strain, 8 weeks) underwent superovulation and mating with
1129 fertile males. Concurrently, recipient females (8 weeks) in estrus were identified via
1130 vaginal smears [45] and paired with vasectomized males. Vaginal plug confirmation at
1131 08:00 the following morning designated gestational day (GD) 0.5. Donors were
1132 euthanized at GD 3.5 (96 hours post-hCG), and blastocysts were flushed from uterine
1133 horns using KSOM embryo culture medium (Sigma, MR-101, USA) maintained at
1134 37°C under 5% CO_2. Pseudopregnant recipients were anesthetized with 1%
1135 pentobarbital sodium. Six morphologically intact blastocysts per uterine horn were
1136 surgically transferred into each uterine horn using a glass transfer pipette (Jitianbio,
1137 JT0061, China). Muscle and skin layers were closed with absorbable sutures (sh-
1138 Jinhuan, R611 6-0, China). Live birth outcomes were recorded daily from GD 19 until
1139 delivery completion.

1140 **Statistics analysis**

1141 Statistical analyses were using GraphPad Prism 10.0 (GraphPad). Data were expressed
1142 as the mean ± SD. Two-tailed unpaired Student's t test and one-way analysis of variance
1143 followed by Tukey's post hoc test were used to analyze the statistical significance
1144 between two groups and among multiple groups, respectively. Chi-squared test was
1145 used in the comparison between the percentages. The statistical significance was set at
1146 P-value < 0.05. Most experiments were repeated at least thrice for reproducibility. The
1147 number of experimental replicates is indicated in the corresponding figure legend. If no
1148 number is listed, the experiment was conducted once.

1149 **DATA AVAILABILITY**

1150 All data are included in the Source data files
1151 (https://doi.org/10.6084/m9.figshare.29878322). The single-cell RNA-seq data reported
1152 in this study have been deposited in the GEO database under accession number
1153 GSE297300. All data are available from the corresponding author upon reasonable
1154 request.

1155 **FUNDING**

1156 This research was supported by the Biological Breeding-Major Projects in National
1157 Science and Technology, Grant/Award Number: 2023ZD04049; Fundamental
1158 Research Funds for the Central Universities (2662023DKPY001) and the National
1159 Natural Science Foundation of China (31701301).

1160 **SUPPORTING INFORMATION**

1161 This article contains supporting information.

1162 **ACKNOWLEDGEMENTS**

1163 We extend our deepest appreciation and respect to Mrs. Fu Bijun, Dr. He's mother, for
1164 her genuine care and encouragement throughout this project.

1165 **AUTHORS' CONTRIBUTION**

C.H. conceived, designed, performed, funded the experiments, analysis the data, and wrote the manuscript; J.L., Q.L., C.L., G.L., and X.L. anticipated in experiment design and conduction, data analysis, and manuscript preparation; X.W., Y.W., R.L., H.W., H.S., Y.Z., W.K., Z.R., Z.W., B.T., C.W., Q.W., G.H and S.Z assisted with sample collection and experiments conduction; C.H., J.L., Q.L., C.L., G.L., and X.L. revised this manuscript. H.C., G.L., and Q.X. supervised this project. All authors approved the final version.

DECLARATION OF INTERESTS

The authors declare that they have no conflicts of interest with the contents of this article.

REFERENCES

1. Niswender, G. D., Juengel, J. L., McGuire, W. J., Belfiore, C. J., & Wiltbank, M. C. (1994). Luteal function: the estrous cycle and early pregnancy. Biology of reproduction, 50(2), 239–247.
2. Stocco, C., Telleria, C., & Gibori, G. (2007). The molecular control of corpus luteum formation, function, and regression. Endocrine reviews, 28(1), 117–149.
3. Practice Committees of the American Society for Reproductive Medicine and the Society for Reproductive Endocrinology and Infertility (2021). Diagnosis and treatment of luteal phase deficiency: a committee opinion. Fertility and sterility, 115(6), 1416–1423.
4. Dimitriadis, E., Menkhorst, E., Saito, S., Kutteh, W. H., & Brosens, J. J. (2020). Recurrent pregnancy loss. Nature reviews. Disease primers, 6(1), 98.
5. Schliep, K. C., Mumford, S. L., Hammoud, A. O., Stanford, J. B., Kissell, K. A., Sjaarda, L. A., Perkins, N. J., Ahrens, K. A., Wactawski-Wende, J., Mendola, P., & Schisterman, E. F. (2014). Luteal phase deficiency in regularly menstruating women: prevalence and overlap in identification based on clinical and biochemical diagnostic criteria. The Journal of clinical endocrinology and metabolism, 99(6), 1007–1014.
6. Baerwald, A., Vanden Brink, H., Hunter, C., Beuker, D., Lim, H., Lee, C. H., & Chizen, D. (2018). Age-related changes in luteal dynamics: preliminary associations with antral follicular dynamics and hormone production during the human menstrual cycle. Menopause, 25(4), 399–407.
7. Weiss G. (2001). Menstrual irregularities and the perimenopause. Journal of the Society for Gynecologic Investigation, 8(1 Suppl Proceedings), S65–S66.
8. Ellison P. T. (1994). Advances in human reproductive ecology. Annual review of anthropology, 23, 255–275.
9. Salazar, E. L., & Calzada, L. (2007). The role of progesterone in endometrial estradiol- and progesterone-receptor synthesis in women with menstrual disorders and habitual abortion.

Gynecological endocrinology : the official journal of the International Society of Gynecological Endocrinology, 23(4), 222–225.

10. Arck, P. C., Rücke, M., Rose, M., Szekeres-Bartho, J., Douglas, A. J., Pritsch, M., Blois, S. M., Pincus, M. K., Bärenstrauch, N., Dudenhausen, J. W., Nakamura, K., Sheps, S., & Klapp, B. F. (2008). Early risk factors for miscarriage: a prospective cohort study in pregnant women. Reproductive biomedicine online, 17(1), 101–113.
11. Jo, M., Brännström, M., Akins, J. W., & Curry, T. E., Jr (2025). New insights into the ovulatory process in the human ovary. Human reproduction update, 31(1), 21–47.
12. Wang, X., Liao, J., Shi, H., Zhao, Y., Ke, W., Wu, H., Liu, G., Li, X., & He, C. (2024). Granulosa cell-layer stiffening prevents escape of mural granulosa cells from the post-ovulatory follicle. Advanced science, 11(33), e2403640.
13. Monaco, C. F., & Davis, J. S. (2023). Mechanisms of angioregression of the corpus luteum. Frontiers in physiology, 14, 1254943.
14. Curry, T. E., Jr, & Smith, M. F. (2006). Impact of extracellular matrix remodeling on ovulation and the folliculo-luteal transition. Seminars in reproductive medicine, 24(4), 228–241.
15. Goldman, S., & Shalev, E. (2004). MMPS and TIMPS in ovarian physiology and pathophysiology. Frontiers in bioscience : a journal and virtual library, 9, 2474–2483.
16. Robker, R. L., & Richards, J. S. (1998). Hormone-induced proliferation and differentiation of granulosa cells: a coordinated balance of the cell cycle regulators cyclin D2 and p27Kip1. Molecular endocrinology, 12(7), 924–940.
17. Jirawatnotai, S., Moons, D. S., Stocco, C. O., Franks, R., Hales, D. B., Gibori, G., & Kiyokawa, H. (2003). The cyclin-dependent kinase inhibitors p27Kip1 and p21Cip1 cooperate to restrict proliferative life span in differentiating ovarian cells. Journal of biological chemistry, 278(19), 17021–17027.
18. Fan, H. Y., Liu, Z., Johnson, P. F., & Richards, J. S. (2011). CCAAT/enhancer-binding proteins (C/EBP)-α and -β are essential for ovulation, luteinization, and the expression of key target genes. Molecular endocrinology, 25(2), 253–268.
19. Fan, H. Y., Liu, Z., Shimada, M., Sterneck, E., Johnson, P. F., Hedrick, S. M., & Richards, J. S. (2009). MAPK3/1 (ERK1/2) in ovarian granulosa cells are essential for female fertility. Science, 324(5929), 938–941.
20. Wu, Y., Ghosh, S., Nishi, Y., Yanase, T., Nawata, H., & Hu, Y. (2005). The orphan nuclear receptors NURR1 and NGFI-B modulate aromatase gene expression in ovarian granulosa cells: a possible mechanism for repression of aromatase expression upon luteinizing hormone surge. Endocrinology, 146(1), 237–246.
21. Salvador, L. M., Maizels, E., Hales, D. B., Miyamoto, E., Yamamoto, H., & Hunzicker-Dunn, M. (2002). Acute signaling by the LH receptor is independent of protein kinase C activation. Endocrinology, 143(8), 2986–2994.
22. Fan, H. Y., Liu, Z., Cahill, N., & Richards, J. S. (2008). Targeted disruption of Pten in ovarian granulosa cells enhances ovulation and extends the life span of luteal cells. Molecular endocrinology, 22(9), 2128–2140.
23. Dinh, D. T., Breen, J., Nicol, B., Foot, N. J., Bersten, D. C., Emery, A., Smith, K. M., Wong, Y. Y., Barry, S. C., Yao, H. H. C., Robker, R. L., & Russell, D. L. (2023). Progesterone

receptor mediates ovulatory transcription through RUNX transcription factor interactions and chromatin remodelling. Nucleic acids research, 51(12), 5981–5996.

24. Meldi, K. M., Gaconnet, G. A., & Mayo, K. E. (2012). DNA methylation and histone modifications are associated with repression of the inhibin α promoter in the rat corpus luteum. Endocrinology, 153(10), 4905–4917.
25. Jeon, H., Choi, Y., Brännström, M., Akin, J. W., Curry, T. E., & Jo, M. (2023). Cortisol/glucocorticoid receptor: a critical mediator of the ovulatory process and luteinization in human periovulatory follicles. Human reproduction, 38(4), 671–685.
26. Pangas S.A., Rajkovic, A. (2015) Chapter 21- follicular development: mouse, sheep, and human Models, in: T.M. Plant, A.J. Zeleznik (Eds.), Knobil and Neill'S Physiology of Reproduction, fourth edition), Academic Press, San Diego, 947–995.
27. Xu, X., Mu, L., Li, L., Liang, J., Zhang, S., Jia, L., Yang, X., Dai, Y., Zhang, J., Wang, Y., Niu, S., Xia, G., Yang, Y., Zhang, Y., Cao, Y., & Zhang, H. (2022). Imaging and tracing the pattern of adult ovarian angiogenesis implies a strategy against female reproductive aging. Science advances, 8(2), eabi8683.
28. Mu, L., Wang, G., Yang, X., Liang, J., Tong, H., Li, L., Geng, K., Bo, Y., Hu, X., Yang, R., Xu, X., Zhang, Y., & Zhang, H. (2025). Physiological premature aging of ovarian blood vessels leads to decline in fertility in middle-aged mice. Nature communications, 16(1), 72.
29. Pereira, M. M., Mainigi, M., & Strauss, J. F. (2021). Secretory products of the corpus luteum and preeclampsia. Human reproduction update, 27(4), 651–672.
30. Mantri, M., Zhang, H. H., Spanos, E., Ren, Y. A., & De Vlaminck, I. (2024). A spatiotemporal molecular atlas of the ovulating mouse ovary. Proceedings of the National Academy of Sciences of the United States of America, 121(5), e2317418121.
31. Rieusset J. (2018). The role of endoplasmic reticulum-mitochondria contact sites in the control of glucose homeostasis: an update. Cell death & disease, 9(3), 388.
32. Chen, J., Zhou, Y., Liu, Z., Lu, Y., Jiang, Y., Cao, K., Zhou, N., Wang, D., Zhang, C., Zhou, N., Shi, K., Zhang, L., Zhou, L., Wang, Z., Zhang, H., Tang, K., Ma, J., Lv, J., & Huang, B. (2024). Hepatic glycogenesis antagonizes lipogenesis by blocking S1P via UDPG. Science, 383(6684), eadi3332.
33. Poulsen, L. C., Bøtkjær, J. A., Østrup, O., Petersen, K. B., Andersen, C. Y., Grøndahl, M. L., & Englund, A. L. M. (2020). Two waves of transcriptomic changes in periovulatory human granulosa cells. Human reproduction, 35(5), 1230–1245.
34. Song, J. L., Wong, J. L., & Wessel, G. M. (2006). Oogenesis: single cell development and differentiation. Developmental biology, 300(1), 385–405.
35. Scoditti, E., Sabatini, S., Carli, F., & Gastaldelli, A. (2024). Hepatic glucose metabolism in the steatotic liver. Nature reviews. Gastroenterology & hepatology, 21(5), 319–334.
36. Hargreaves, M., & Spriet, L. L. (2020). Skeletal muscle energy metabolism during exercise. Nature metabolism, 2(9), 817–828.
37. Devall, A. J., & Coomarasamy, A. (2020). Sporadic pregnancy loss and recurrent miscarriage. Best practice & research. Clinical obstetrics & gynaecology, 69, 30–39.
38. Coomarasamy, A., Devall, A. J., Brosens, J. J., Quenby, S., Stephenson, M. D., Sierra, S., Christiansen, O. B., Small, R., Brewin, J., Roberts, T. E., Dhillon-Smith, R., Harb, H., Noordali, H., Papadopoulou, A., Eapen, A., Prior, M., Di Renzo, G. C., Hinshaw, K., Mol, B. W., Lumsden, M. A., … Gallos, I. D. (2020). Micronized vaginal progesterone to

prevent miscarriage: a critical evaluation of randomized evidence. American journal of obstetrics and gynecology, 223(2), 167–176.

39. Carp H. J. A. (2020). Progestogens in luteal support. Hormone molecular biology and clinical investigation, 42(2), 143–148.
40. Garg, A., Zielinska, A. P., Yeung, A. C., Abdelmalak, R., Chen, R., Hossain, A., Israni, A., Nelson, S. M., Babwah, A. V., Dhillo, W. S., & Abbara, A. (2024). Luteal phase support in assisted reproductive technology. Nature reviews. Endocrinology, 20(3), 149–167.
41. Duran J, Saez I, Gruart A, Guinovart JJ, Delgado-García JM. (2013). Impairment in long-term memory formation and learning-dependent synaptic plasticity in mice lacking glycogen synthase in the brain. J Cereb Blood Flow Metab. 33(4):550-6.
42. Fan HY, Shimada M, Liu Z, Cahill N, Noma N, Wu Y, Gossen J, Richards JS. (2008). Selective expression of KrasG12D in granulosa cells of the mouse ovary causes defects in follicle development and ovulation. Development. 135(12):2127-37.
43. Blondel, V. D., Guillaume, J.-L., Lambiotte, R., & Lefebvre, E. (2008). Fast unfolding of communities in large networks. Journal of Statistical Mechanics: Theory and Experiment, 2008(10), P10008.
44. Lowe ME. (1992). Site-specific mutations in the COOH-terminus of placental alkaline phosphatase: a single amino acid change converts a phosphatidylinositol-glycan-anchored protein to a secreted protein. J Cell Biol. 116(3):799-807.
45. Zhang Z, He C, Gao Y, Zhang L, Song Y, Zhu T, Zhu K, Lv D, Wang J, Tian X, Ma T, Ji P, Cui W, Liu G. (2021). α-ketoglutarate delays age-related fertility decline in mammals. Aging Cell. 20(2):e13291.